DOI: 10.1002/anie.200601678

Solid-State Structures

Interpenetrating Polar and Nonpolar Sublattices in Intermetallics: The $NaCd_2$ Structure

Daniel C. Fredrickson, Stephen Lee, and Roald Hoffmann**

Keywords:
chemical bonding · crystallography · intermetallic phases · molecular-orbital calculations · solid-state structures

Dedicated to Professor Wolfgang Jeitschko on the occasion of his 70th birthday

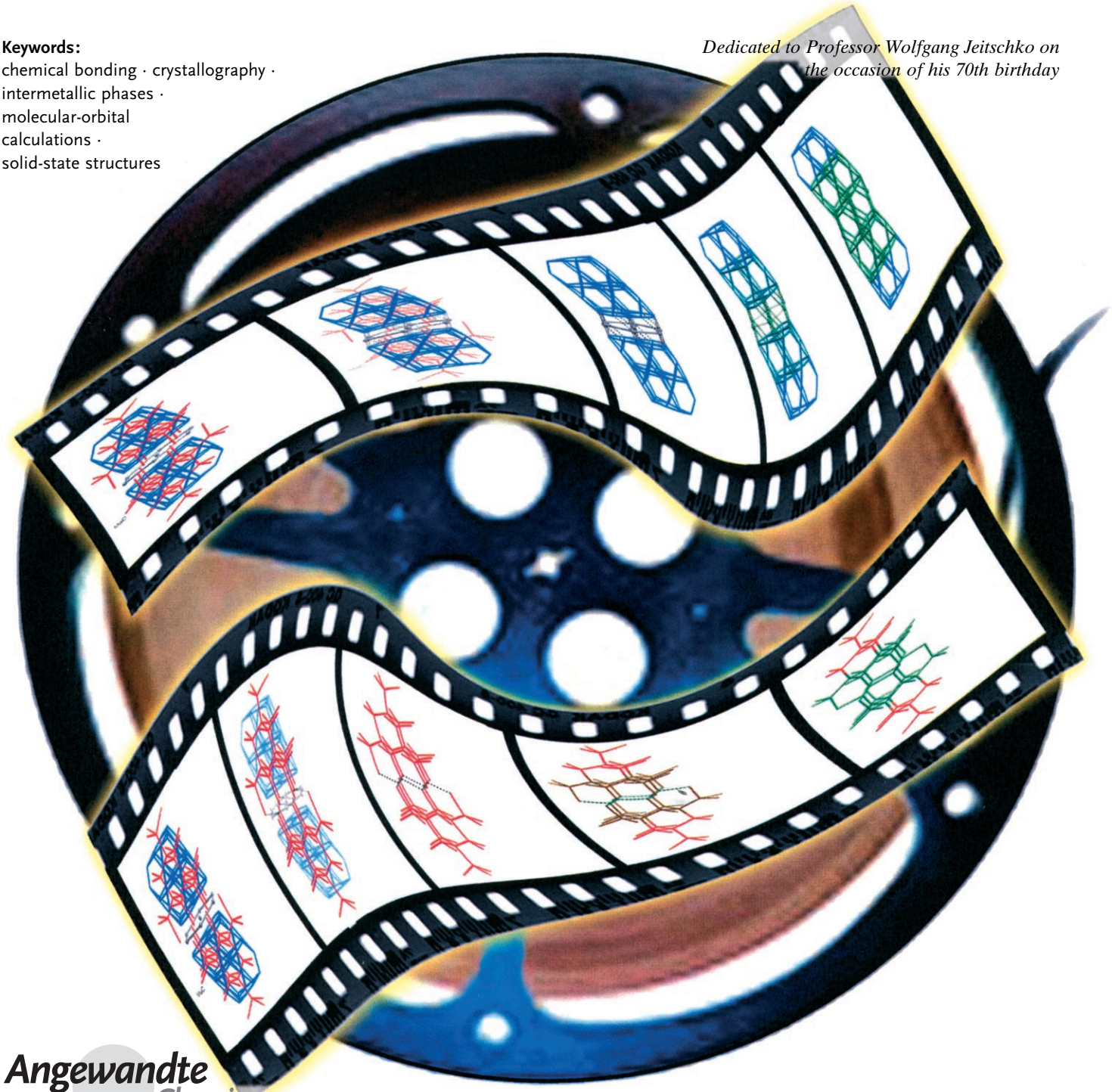

In the 1960s, Samson solved the structures of some of the most complicated intermetallic phases known, including those of $NaCd_2$, Mg_2Al_3, and Cu_3Cd_4 (each with over 1000 atoms per unit cell). Following remarkable earlier constructions by Samson and by Andersson, we use quantum-mechanical calculations as a guide to describing and understanding these structures. Our electronic Aufbau begins with the relatively simple $Mg_{17}Al_{12}$ structure and works up to Samson's $NaCd_2$ structure. In both structures, a division of the sites into electron-rich and electron-poor (with respect to an average electron count) reveals $MgCu_2$-type fragments. Between the interiors and exteriors of these fragments, a change in bonding character takes place—the interiors are more polar, the interfaces relatively nonpolar. This electronic situation is traced to the geometry of the interface sites; they lie simultaneously on electron-rich and electron-poor networks. The resulting polar and nonpolar sites in $NaCd_2$ are separated by a minimal surface, the D surface. The driving force for assuming this structure is electronic: $NaCd_2$ features an interpenetration of polar and nonpolar bonding regions. This sort of thinking can be applied to other structures.

From the Contents

1. Simple Stoichiometries, Complex Structures

Why do intermetallics sometimes have plain structures, and sometimes immensely complicated ones? Take for example the Mg–Al binary system.[1] The stable phases include simple structures, such as face-centered cubic (fcc) and hexagonal close-packed (hcp) alloys, and two structures of moderate complexity, those of $Mg_{17}Al_{12}$ (an ordered binary variant of the α-Mn structure type)[2] and $Mg_{23}Al_{30}$.[3] And then there is a phase referred to optimistically as Mg_2Al_3; it's reported to have roughly 1168 atoms in its cubic unit cell![4]

Phases of like complexity have been found over the past 60 years or so by Samson, Pauling, Shoemaker, and others—a selection of cubic examples is given in Table 1.[5–20] Some of them have been recognized as quasicrystal approximants.[21,17,22,19] The community has struggled impressively to make sense of these structures with descriptions ranging from complex tetrahedral close packings of spheres[23,24] to congeries of concentric or fused polyhedra or interpenetrating frameworks.[25–31] Beautiful clusters of clusters of icosahedral and tetrahedral polyhedra emerge from these analyses.

As an example, we show in Figure 1 one way Samson described his Mg_2Al_3 and $NaCd_2$ structures.[32,33] He started out with a pentagonal complex of Friauf polyhedra (Figure 1a,b) and then joined the pentagonal complexes together to form a larger octahedral cluster (Figure 1c). The full structures (Figure 1d) can then be comprehended in terms of this 234-atom unit.

The Friauf polyhedron is a recurring feature in efforts to describe other complex intermetallic structures as well. In what we perceive as the most insightful of these efforts, Andersson saw components of simpler intermetallic structure types in Samson's Cu_3Cd_4 structure. He found that the Friauf polyhedra were fused to form blocks of the $MgCu_2$ structure type, intergrown with fragments of the pyrochlore and fcc structure types.[45] Andersson and co-workers later showed that the $MgCu_2$-type blocks present in the Cu_3Cd_4 structure also occur in the giant structures of $NaCd_2$ and Mg_2Al_3,[46] which we illustrate in Figure 1.

None of these phases is a comfortable haven for lovers of simplicity.

The geometry of nature never ceases to astound, nor does the ingenuity of human beings (cited only in part above) in discerning patterns. To this, the intermetallics in question

[*] Dr. D. C. Fredrickson,[+] Prof. S. Lee, Prof. R. Hoffmann
Department of Chemistry and Chemical Biology
Baker Laboratory
Cornell University
Ithaca, NY 14853-1301 (USA)
Fax: (+1) 607-255-4137
E-mail: sl137@cornell.edu
rh34@cornell.edu

[+] Present address: Department of Inorganic Chemistry Stockholm University 106 91 Stockholm (Sweden)

Supporting information for this article is available on the WWW under http://www.angewandte.org or from the author.

Table 1: Examples of cubic phases based on Laves phase type fragments.

Compound	*a* [Å]	Space group
$NaCd_2$[32]	30.56	$Fd\bar{3}m$
Mg_2Al_3[4]	28.32	$Fd\bar{3}m$
Cd_4Cu_3[34]	25.87	$F\bar{4}3m$
$K_{17}In_{41}$[35]	24.24	$Fd\bar{3}m$
Na_6Tl[36]	24.15	$F\bar{4}3m$
$Na_{28}In_{14}Sn_{15}$[37]	22.99	$F\bar{4}3m$
$Na_{17}In_{12}Ga_{29}$[38]	21.79	$Fd\bar{3}m$
$Sm_{11}Cd_{45}$[39]	21.70	$F\bar{4}3m$
$Na_{35}Cd_{24}Ga_{56}$[40]	21.29	$F\bar{4}3m$
$Li_{18}Cu_5In_4Ga_{31}$[41]	19.93	$Fd\bar{3}m$
$FeNiZn_{13}$[13]	18.08	$F\bar{4}3m$
$Cu_{41}Sn_{11}$[42]	17.98	$F\bar{4}3m$
$Fe_{22}Zn_{48}$[43]	17.96	$F\bar{4}3m$
$CaNa_{10}Sn_{12}$[44]	11.22	$F\bar{4}3m$
$Mg_{17}Al_{12}$[2]	10.54	$Fd\bar{3}m$

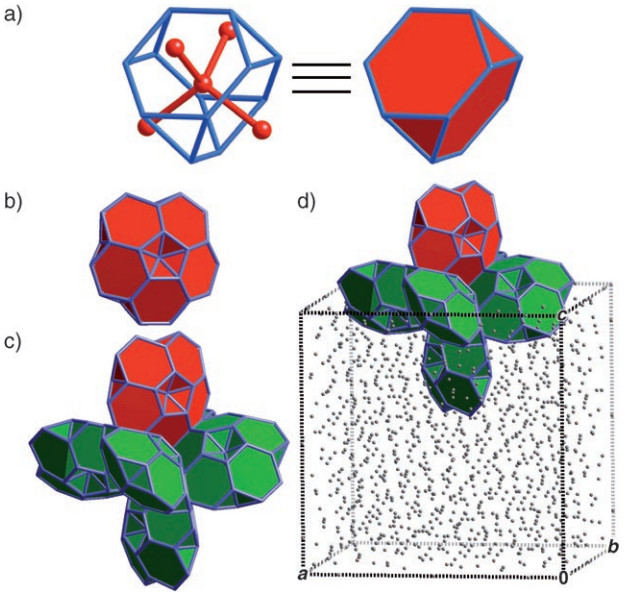

Figure 1. Samson's construction of the Mg_2Al_3 and $NaCd_2$ structures. a) The Friauf polyhedron, which comprises fragments of diamondoid (red spheres) and truncated-tetrahedral (blue) networks. b) The pentagonal complex of five face-sharing Friauf polyhedra. c) The octahedral unit built from six of these pentagonal complexes joined in an edge-sharing fashion. d) This unit in the context of the full unit cell of the $NaCd_2$ structure. See this Figure animated in the Supporting Information.

testify gloriously. The question remains how relevant these geometrical schemes, beautiful as they are, might be to the *bonding* in these phases. Geometry and electronics must be interrelated—the chemical universe is both classical and quantum-mechanical. The Hume-Rothery rules[47–49] (and their electronic justification) are one attempt to introduce electronic reasoning in the intermetallic realm.[50] In another approach, modified Wade–Mingos polyhedral bonding schemes have been used to make sense of the electron counts in some complex structures featuring polyhedra.[51] Examples are the lovely analyses of the $Na_{35}Cd_{24}Ga_{56}$ structure type by Tillard-Charbonnel and Belin,[40] and $K_{17}In_{41}$-type compounds by Lin and Corbett.[52]

In this paper, we will take a fresh view of these complex intermetallic structures, growing out of quantum-mechanical calculations. An analysis of a measure of electron distribution, or charging, the Mulliken electron populations, will reveal large blocks of a simple structure, the $MgCu_2$ type, in phases such as $NaCd_2$. We will see that the complex phases of Table 1 can be understood both geometrically *and* electronically as chemical twinnings of the $MgCu_2$ structure type.

Geometrically, we will have arrived at this point at a scheme similar to that proposed by Andersson. But our path, based as it is on quantum mechanics, provides the electronic underpinnings of Andersson's fertile vision of intricate structures constructed from simpler ones.[45,53] Also, the story does not end simply with $MgCu_2$-type blocks. Our calculations point to a transition between polar bonding within the blocks and nonpolar bonding in the interface regions.

2. Underlying Phases and Blurred Identities

We begin our journey toward $NaCd_2$ with two quite common intermetallic structure types, those of the Laves phases $MgCu_2$ and $MgZn_2$.[54] Underlying both structures are tetrahedral networks built from the Mg atoms (red in Figure 2 a,c). In $MgCu_2$, the Mg atoms trace out the cubic diamond structure, while in $MgZn_2$ they form the hexagonal diamond structure. Cu or Zn atoms surround each Mg atom to form truncated tetrahedra (blue in Figure 2). The truncated tetrahedra of neighboring Mg atoms share faces to create an extended network of truncated tetrahedra, which, together with shared smaller tetrahedra, fills space. Friauf polyhedra, the fundamental building blocks of Samson's structures, arise

Daniel Fredrickson developed a fascination with the connection between structure and orbital interactions while an undergraduate at the University of Washington, Seattle, where he worked under the supportive guidance of Bart Kahr. As a graduate student at Cornell University, he explored this connection in the groups of Stephen Lee and Roald Hoffmann. He is currently trying his hand at the experimental side of taming complex intermetallic phases as a postdoctoral researcher with Sven Lidin at Stockholm University.

Stephen Lee's abiding interest with intermetallic crystals dates back to his training with Jeremy Burdett, Jean Rouxel, and Wolfgang Jeitschko. Since 1998, he has been a Professor in the Chemistry and Chemical Biology Department of Cornell University.

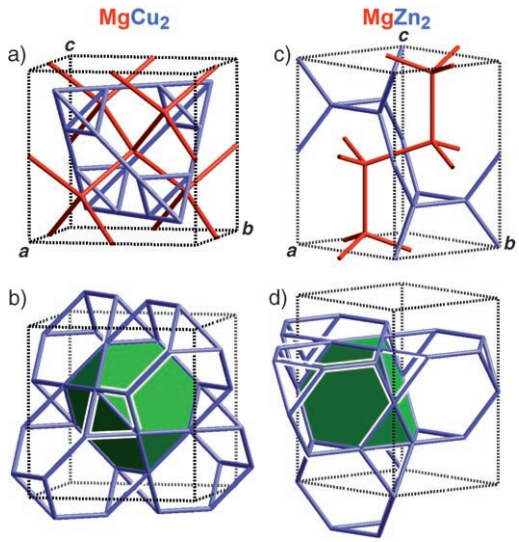

Figure 2. The $MgCu_2$ and $MgZn_2$ structure types. a) A single unit cell of the $MgCu_2$ structure type. b) The Cu network of face-sharing truncated tetrahedra in $MgCu_2$, with one of these polyhedra emphasized in green. c) A single unit cell of the $MgZn_2$ structure type. d) The Zn network of face-sharing truncated tetrahedra in $MgZn_2$, with one of these polyhedra emphasized in green. See this Figure animated in the Supporting Information.

from this superposition of $Mg(Mg)_4$ tetrahedra and truncated tetrahedra.

In both the $MgCu_2$ and $MgZn_2$ structures, the sites are divided simply into ones that lie on truncated-tetrahedral networks (TT sites) and those that lie on diamondoid networks (D sites). In more complex structures containing Friauf polyhedra, an intriguing ambiguity in the assignment of atoms to clusters and networks creeps in.[55] A simple example of this ambiguity occurs in the $Mg_{17}Al_{12}$ structure,[2] an ordered variant of the α-Mn structure type, shown in Figure 3. The structure is based on a body-centered packing of Friauf polyhedra (with Al on the TT sites, Mg on the D sites). This description accounts for three of the four symmetry-distinct sites (TT, D1, and D2).

The remaining site, a Mg site labeled D3 in Figure 3, can be attached, conceptually, to the original Friauf polyhedra in a variety of ways. One alluring choice is shown in Figure 3b, in which we draw bonds for the (much) longer of the two types of D3–D2 (Mg–Mg) contacts (ca. 3.4 vs. 3.0 Å). These new D3–D2 contacts extend the central $Mg(Mg)_4$ tetrahedron to

Roald Hoffmann was born in Złoczów, Poland, now Zolochiv, Ukraine. His father was a civil engineer who built roads and bridges near his hometown. Perhaps that is whence Roald's inclination for searching for ways to understand, for structure, and for building bridges between all branches of chemistry (and beyond) derives. Or perhaps it comes from having survived the war. Relevant to this paper, he is the scientific grandchild of Linus Pauling, who was Sten Samson's mentor, and he spent a half year in Sten Andersson's group.

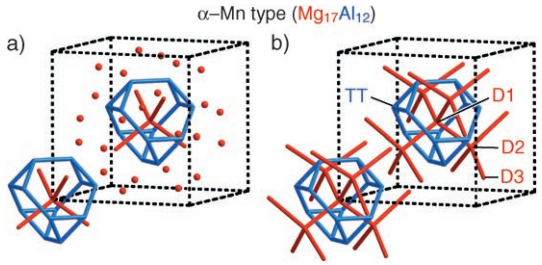

Figure 3. The $Mg_{17}Al_{12}$ structure. a) Friauf polyhedra in this structure. b) One possible way of using the remaining atoms at the D3 site to extend the truncated-tetrahedral (blue) and diamondoid (red) networks of the Friauf polyhedra. This choice was made to stress the relationship between this structure and the $MgCu_2$ structure type (Figure 2a). The site labels used in Table 2 are also given. See this Figure animated in the Supporting Information.

form a piece of the cubic diamond structure. Together with the Al truncated tetrahedron, this extended diamondoid network forms a fragment of the $MgCu_2$ structure type. From this point of view, the $Mg_{17}Al_{12}$ structure then consists of a body-centered packing of $MgCu_2$-type fragments.

Other possibilities for assigning the D3 site are shown in Figure 4, using the shorter Mg–Mg contacts. We begin with two of the $MgCu_2$-type fragments drawn in Figure 3a and then look for additional contacts to the D3 sites which extend the networks of the original Friauf polyhedron. We draw in those contacts extending the truncated-tetrahedral networks with blue dotted lines. These dotted lines, in fact, trace out a new truncated tetrahedron linking the original clusters! Indeed, this polyhedron is part of a full Friauf polyhedron centered on the D2 site, emphasized with thick solid bars in Figure 4b. In this new Friauf polyhedron, the D3 site plays double duty, as can be seen by the positions of the red spheres in Figure 4b.[26] Three of the six D3 sites lie on the truncated tetrahedron of the nascent Friauf polyhedron, the remaining three on the diamondoid network.

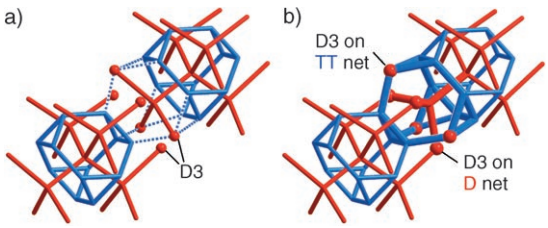

Figure 4. Alternative assignments of the D3 site in the $Mg_{17}Al_{12}$ structure to the diamondoid (D) or truncated-tetrahedral (TT) networks. a) Two adjacent $MgCu_2$-type fragments in the $Mg_{17}Al_{12}$ structure. The D3 sites are indicated with red spheres. Blue dotted lines show close contacts to the D3 sites which extend the truncated-tetrahedral networks of the $MgCu_2$-type fragments. b) These contacts create a Friauf polyhedron (thick bars) at the interface between the $MgCu_2$-type fragments, with the D3 site atoms participating on both the truncated-tetrahedral and diamondoid networks. See this Figure animated in the Supporting Information.

So … an identity crisis. Is there some way to assign these D3 sites more systematically? For instance, could we use the "analog computer" of the structure itself, the choice made by

the Al or Mg atoms for one or another site, the "coloring" of the structure's sites? It turns out that the D3 site is occupied by Mg, along with the D1 and D2 sites (though, as Samson mentioned, partial occupation of the D3 site by Al could lead to the observed phase width for this structure[26]). Following this observation, we tentatively classify the D3 site with the other D sites.

Now that we've covered the geometrical aspects of the Laves phases $MgCu_2$ and $MgZn_2$, and the $Mg_{17}Al_{12}$ structure, let's see how these *geometrical* characteristics are related to essential features of their *electronic* structures.

3. Linking Geometry to Electronic Structure

To make connections between geometrical and electronic structure most clear, we will focus on hypothetical alloys with random or "averaged" Mg/Cu, Mg/Zn, or Mg/Al occupation of all of the sites. Such models, while unrealistic, provide the way in to reasons for real site occupancy.[56–61] For a given average electron count, there is a natural (origin to be determined) differential in the electron population of atoms residing in sites that are distinct by symmetry. As was observed as far back as 1950 by Longuet-Higgins and co-workers, the more electronegative atoms in a real compound tend to choose the sites with the highest electron populations in a parent "averaged" structure.[56] This correlation between electron populations calculated for a disordered reference structure and the experimentally observed site preferences was later termed "topological charge stabilization" by Gimarc.[57] This is not the only way calculations on averaged structures can reveal information about site occupancies; Franzen and Köckerling have used overlap populations from similar calculations to make sense of mixed-occupancy trends, for instance, the partial ordering of the Nb and Ta atoms in Nb–Ta sulfides.[58]

To implement this way of thinking, we calculated the band structures for both the $MgCu_2$ and $Mg_{17}Al_{12}$ structure types, using the extended Hückel (eH) method (we also did density functional theory (DFT) calculations with the local-density approximation (LDA) to calibrate our eH parameters; see Appendix), modeling the averaged alloy by putting Al atoms on *all* the sites and adjusting the overall charge per unit cell to match the average electron count of $Mg_{17}Al_{12}$ (i.e., $(17\times2+12\times3)/29=70/29=2.41$ electrons per atom). The site electron densities were then computed by a Mulliken population analysis.

The resulting electron populations are shown in Figure 5. In Figure 5a and d, the two structures are given with the relative Mulliken population (the deviation from the average number of electrons per atom) written in for each site.[59] For both structures, the D sites (red) carry less-than-average electron density; they are electron-poor. The sites on truncated tetrahedra (blue) are consistently electron-rich.

These results are illustrated in another, perhaps more graphic, way in Figure 5b and e. The signs of the relative Mulliken populations are indicated by the color of the spheres: black for atoms that are relatively electron-poor, and white for atoms that are electron-rich compared to the average. Thus, the diamondoid networks of both the $Mg_{17}Al_{12}$ and $MgCu_2$ structures are seen in these pictures as black beads connected via red lines. The TT sites appear as white spheres connected by blue lines. The volumes of the spheres give the magnitudes of their relative Mulliken populations (sites with

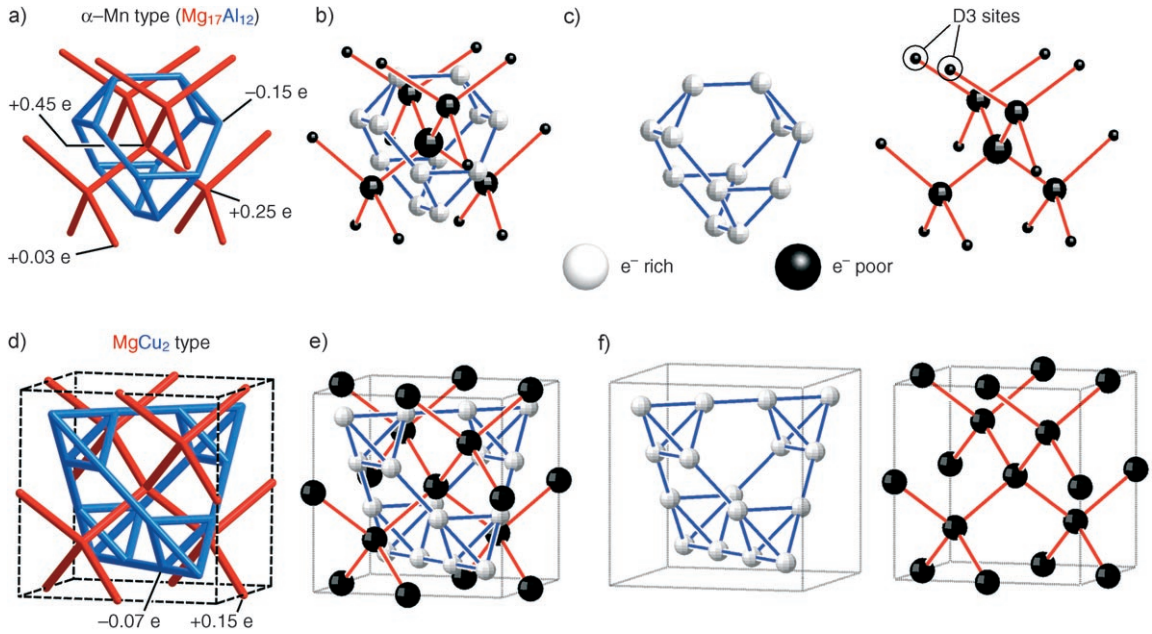

Figure 5. Relative Mulliken electron populations in a)–c) the $Mg_{17}Al_{12}$ structure and d)–f) the $MgCu_2$ structure type. In (a) and (d), the relative populations of the sites are written out numerically; in (b), (c), (e), and (f), the relative populations are plotted as spheres. The sphere volume gives the absolute value of that site's relative population, while the sphere color indicates the sign of the relative population. White: electron-rich compared to the average electron count; black: electron-poor. In (c) and (f), the networks formed from the electron-rich (right) and electron-poor (left) sites are shown separately. See this Figure animated in the Supporting Information.

electron counts very close to the average appear with spheres of zero radius, that is, no sphere). *These conventions will be used throughout this paper.*

From the electronic perspective, we arrive at a different vantage point on the structural ambiguity of the $Mg_{17}Al_{12}$ D3 site (circled in Figure 5c). We saw that this site could be assigned to either the truncated-tetrahedral or diamondoid parts of the structure, depending on which bonds we drew (and which we did not). In line with this ambiguity, the relative Mulliken population is small (meaning a close-to-average electron count). Whereas the Mulliken populations for the other sites in the $Mg_{17}Al_{12}$ structure have increased in magnitude over their corresponding sites in the $MgCu_2$ structure, the value for the D3 site has shrunk.

The experimental site orderings of compounds adopting the α-Mn (e.g., $Mg_{17}Al_{12}$) and $MgCu_2$ structure types are consistent with the computed average electron densities. It is well-known that for compounds crystallizing in the $MgCu_2$ type, the electropositive atoms (the less electronegative atoms in the structure) and electronegative atoms segregate preferentially to, respectively, the Mg and Cu sites. Of the more than 228 AB_2 binary compounds of the $MgCu_2$-type, there are only nine cases where the A atom exceeds the B atom in electronegativity.[62]

In Table 2, we show the site preferences for binary compounds crystallizing in the α-Mn type with observed site orderings (many α-Mn-type compounds are alloys in which no site orderings have been detected). This list has been recently compiled by Fässler and co-workers, in the course of their investigations of site ordering in their compound K_5Pb_{24}.[63] We label the four symmetry-distinct sites in these structures as TT and D1–D3, as was shown in Figure 3. In all these cases, the TT positions are occupied by the more electronegative element. However, the stoichiometries in most of these compounds do not allow for a clean separation of elements between the TT and D sites. The remaining atoms of the more electronegative element are accommodated by the D3 site, the most electron-rich D site (followed, in the case of the Y–Mg structures, by the D1 and D2 sites).

Table 2: Site orderings in binary compounds adopting the α-Mn structure type (after Fässler et al.).[63]

Compound	D1[a]	D2	D3	TT
Er_5Mg_{24}[64]	1 Er	4 Er	12 Mg	12 Mg
$Mg_{17}Al_{12}$[2]	1 Mg	4 Mg	12 Mg	12 Al
K_5Pb_{24}[63]	1 K	4 K	12 Pb	12 Pb
$NbRe_3$[65]	1 Nb	4 Nb	2.26 Nb/9.74 Re	12 Re
Sc_5Re_{24}[66]	1 Sc	4 Sc	12 Re	12 Re
Ti_5Re_{24}[67]	1 Ti	4 Ti	12 Re	12 Re
Tm_5Mg_{24}[64]	1 Tm	4 Tm	12 Mg	12 Mg
$YMg_{6.8}$[68]	1 Y	2.72 Y/1.28 Mg	12 Mg	12 Mg
Y_5Mg_{24}[69]	0.25 Mg/0.75 Y	4 Y	12 Mg	12 Mg

[a] See Figure 3b for site labels.

4. On the Way to the $NaCd_2$ Structure

4.1. $MgCu_2$-Type Clusters

The preceding electronic analysis highlights a key difference between the $MgCu_2$ and α-Mn structure types. The Mulliken populations of the $MgCu_2$ structure type indicate that it is comprised of an electron-rich truncated-tetrahedral net interpenetrated by an electron-poor diamondoid net. Both nets are extended; from Friauf polyhedron to Friauf polyhedron, the bond polarity remains uniform. In the α-Mn structure type, however, the bond polarity loses this uniformity: individual polar Friauf polyhedra are isolated from each other by a layer that is nonpolar (near-zero relative Mulliken populations). The structure then consists of polar blocks immersed in a nonpolar matrix.

With these lessons in hand, let's look at two of the most complex phases in the intermetallic literature: the $NaCd_2$ and Mg_2Al_3 structures. Both structures were solved in the 1960s, and as truly heroic feats of crystallography as they remain, the quality of the structure determinations suffers from the limitations of the technology of the time. The Mg_2Al_3 structure exhibits partial occupancies and disorder that mar any attempt at quantum-mechanical calculations or structural description of the phase. The $NaCd_2$ structure is much less troubled by disorder (at least in the current structure solutions),[70] with just some sites showing partial occupancy by Cd or mixed occupancy by Na and Cd, so we'll start with it.

Our approach to this structure is to look at the separate networks formed by the electron-poor and electron-rich sites, as revealed by electronic structure calculations. Just as we did for the α-Mn and $MgCu_2$ structure types above, we will examine the relative Mulliken populations for a hypothetical unordered Na–Cd alloy taking on the $NaCd_2$ structure type, setting the electron count to match that of Andersson's structure solution, 1.63 electrons per atom (see Appendix).

Two fragments of different sizes come into focus as we enter the full complexity of the $NaCd_2$ structure from the electronic perspective. These are ordered groupings of atoms we will call, respectively, the "major" and "minor" clusters (Figure 6). Both are of tetrahedral symmetry, being centered on tetrahedral Wyckoff positions in the *F*-centered cubic unit cell. We will see below that all of the atoms in the $NaCd_2$ unit cell either lie on one of these two types of clusters or on the thin interfaces between these clusters.

The reader should be aware that we use the word "cluster" in a slightly nonstandard way. The clusters identified in $NaCd_2$ are arrays of atoms, with a recognizable local connectivity. But they are not isolated; they are cluster building blocks of a lattice, connecting up with other clusters to form a network.[71]

The major cluster is shown in detail and from a friendlier perspective in Figure 7, with Figure 7a–c focusing on the geometry of the cluster, and Figure 7d–f focusing on the Mulliken populations. It consists of 10 Friauf polyhedra joined through sharing hexagonal faces of their truncated tetrahedra (blue). In the act of sharing faces, small tetrahedra are created, just as in the $MgCu_2$ structure type. This is shown in Figure 7b, where it may be seen that the small tetrahedra share vertices to create a tetrahedron of these smaller

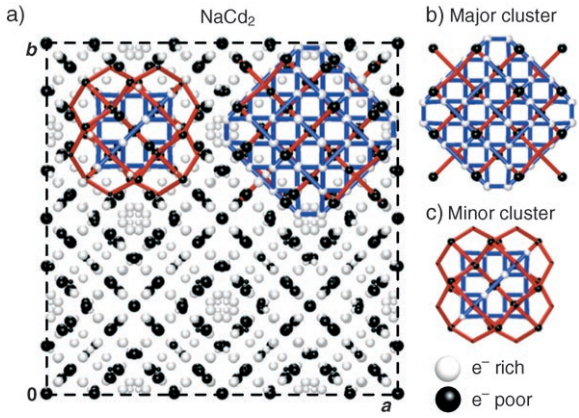

Figure 6. Fragments of the $MgCu_2$ type in the $NaCd_2$ structure revealed through relative Mulliken populations. a) Relative Mulliken populations plotted for the whole $NaCd_2$ unit cell. b) The larger $MgCu_2$-type fragment, which we term the major cluster. c) The smaller $MgCu_2$-type fragment, the minor cluster. See the caption to Figure 5 for conventions on plotting relative Mulliken populations, and Figures 7 and 8 for detailed views of the major and minor clusters, respectively. See this Figure animated in the Supporting Information.

tetrahedra. In the fusion of these Friauf polyhedra, the atoms shown in red interconnect (Figure 7c). The innermost atoms of the resulting fragment trace out an adamantane frame, a hallmark of the cubic diamond structure. Further atoms are added to complete the tetrahedral coordination of each atom of the adamantane piece. In short, the fusion of Friauf polyhedra to make the major cluster produces a truncated version of the Mg and Cu networks in $MgCu_2$; the major cluster can be simply understood as a fragment of the $MgCu_2$ structure type.

This structural similarity of the major cluster to $MgCu_2$ is reflected in the distribution of the Mulliken populations (Figure 7d–f): the truncated-tetrahedral network (analogous to the Cu network in $MgCu_2$) is electron-rich (Figure 7e), while the diamondoid network (analogous to the Mg network in $MgCu_2$) is electron-poor (Figure 7f).

The minor cluster is also derived from the $MgCu_2$ structure type (Figure 8a–c). It consists of a single Friauf polyhedron, with additional atoms building up the cluster. Some of the additional atoms extend the diamondoid network branching from the center of the cluster (in the process, four adamantane-type pieces, sharing edges, are made), mimicking the Mg substructure of the $MgCu_2$ structure type. The other atoms cap the triangular faces of the truncated tetrahedron extending the Cu network of the $MgCu_2$ structure type. In Figure 8d, we show the Mulliken populations for the minor clusters. As with the major cluster, a clear separation of electron-rich and electron-poor sites occurs: the TT sites are electron-rich, the D sites electron-poor.

4.2. Site Occupancies in $NaCd_2$

How do these eH Mulliken populations compare with the experimentally determined site occupancies? Guided by topological charge stabilization ideas, we should see a

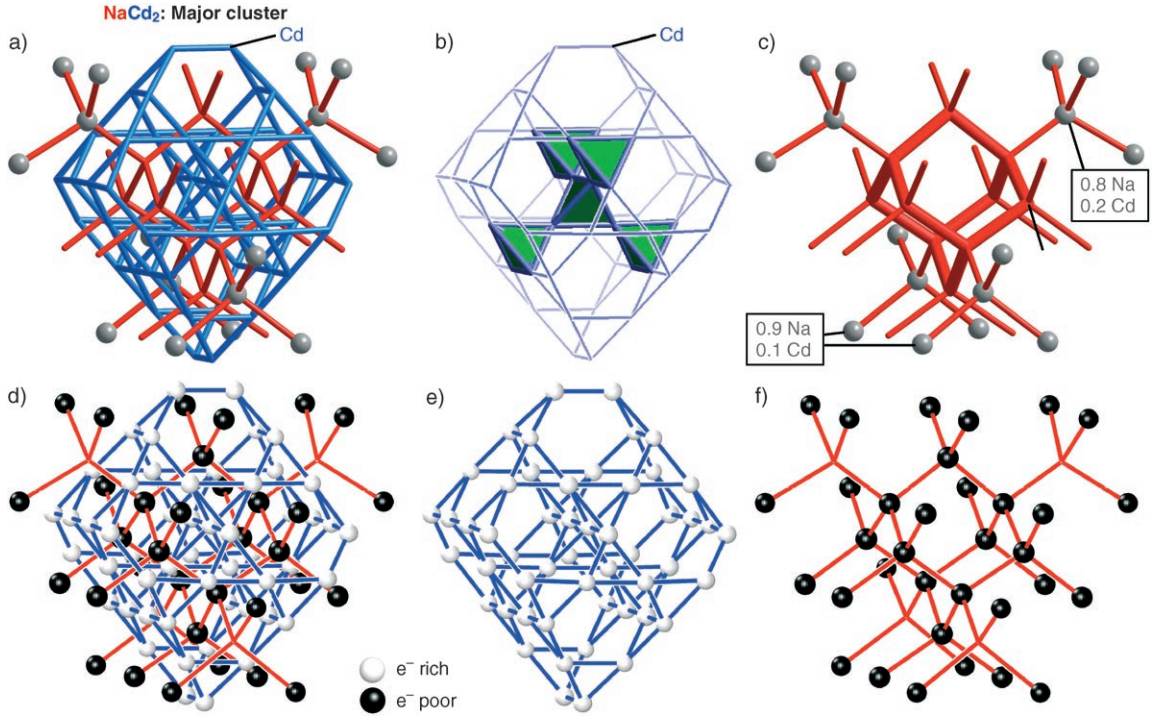

Figure 7. The major cluster in the $NaCd_2$ structure with the site occupancies from Andersson's solution. a) The full cluster. b) The truncated-tetrahedral fragment, consisting of Cd atoms. c) The diamondoid fragment, consisting mainly of Na atoms. d) The relative Mulliken populations of the major cluster. e) The electron-rich sites form nets based on truncated tetrahedra and smaller tetrahedra, as in the Cu substructure of the $MgCu_2$ structure type. f) The electron-poor sites trace out tetrahedral frameworks, reminiscent of the Mg diamondoid nets in the $MgCu_2$ structure type. See the caption to Figure 5 for conventions on plotting relative Mulliken populations. See this Figure animated in the Supporting Information.

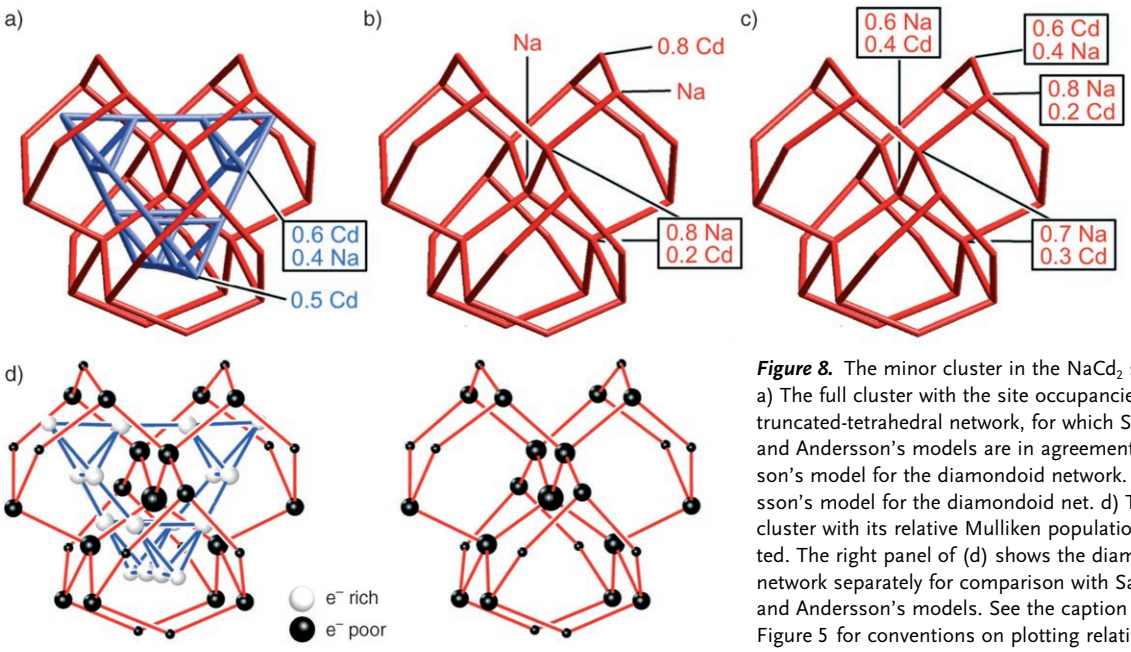

Figure 8. The minor cluster in the $NaCd_2$ structure. a) The full cluster with the site occupancies for the truncated-tetrahedral network, for which Samson's and Andersson's models are in agreement. b) Samson's model for the diamondoid network. c) Andersson's model for the diamondoid net. d) The minor cluster with its relative Mulliken populations plotted. The right panel of (d) shows the diamondoid network separately for comparison with Samson's and Andersson's models. See the caption to Figure 5 for conventions on plotting relative Mulliken populations. See this Figure animated in the Supporting Information.

predominant occupation of the D sites by the electropositive Na atoms and occupation of the TT sites by the relatively electronegative Cd atoms. For the major cluster, this is indeed what we see (Figure 7a–c). All of the TT sites (blue) are exclusively occupied by Cd. All but two of the D sites (red) are occupied by Na. The exceptions are two sites at the outskirts of the cluster with mixed occupancy: one is essentially a Na site (0.9 Na, 0.1 Cd); the other is much more Cd-rich (0.8 Cd, 0.2 Na). Remarkably, the site occupancies and Mulliken populations agree in these exceptions to the rule: the one site occupied mainly by Cd atoms on the diamondoid net is marginally electron-rich, while the one showing weak Cd occupation has is the least electron-poor of the remaining D sites.

The ordering of the Na and Cd atoms in the minor cluster is not nearly so clean. In Figure 8a–c, we compare the site occupancies in Samson's and Andersson's structural models. Mixed and partial occupancies are common to both structures. The Na/Cd pattern in the truncated-tetrahedral network is essentially the same in the two solutions (Figure 8a). Differences between the two structural solutions occur in the diamondoid networks: Samson's model has the diamondoid network predominantly occupied by Na atoms (Figure 8b), while in Andersson's model, the Na/Cd mixed occupancy on the diamondoid network is more pronounced (Figure 8c). Samson's model is more in accord with our earlier observations that the diamondoid networks of $MgCu_2$-type fragments tend to be electropositive.

From the Mulliken populations, however, we can rationalize some features of the minor cluster Na/Cd orderings in the experimental solutions. For instance, we might expect some Cd occupancy on the two-coordinate D sites of Figure 8d, with their very small spheres indicating near-average electron counts. These sites are occupied predominantly by Cd in both structure solutions (Figure 8b,c).

The close agreement between semiquantitative theory and experiment for the major cluster makes one wonder about the discrepancies seen experimentally for the minor cluster. One possibility is that the ratio of D to TT sites in the $NaCd_2$ structure cannot adequately accommodate the 1:2 Na/Cd ratio. 544 of the 1192 atoms in the unit cell lie on the TT sites of the major and minor clusters, 536 on the D sites, and 112 in interstices. With the TT sites comprising less than half of the sites, but roughly two-thirds of the atoms being Cd, we should expect to see some of the Cd atoms spilling over into the D sites. One of the referees of this paper suggests that an entropic contribution may also be at work here and in the other cases of disorder occurring in the Samson phases—an effect which is not considered in our Mulliken population based approach. We will see below that the discrepancies can be traced to a structural ambiguity analogous to that we saw earlier for the D3 site in $Mg_{17}Al_{12}$.

4.3. $NaCd_2$ in All its Glory

The full $NaCd_2$ structure is built from a packing of the major and minor clusters together (as dictated by the *F* centering and *d*-glide planes of this structure's space group, $Fd\bar{3}m$). It's easiest to visualize this process by first looking at the arrangement of the two clusters in the unit cell separately, then combining them. This is shown in Figure 9, where we start with the packing of the minor cluster (Figure 9a). In this Figure, we "abbreviate" for the sake of clarity the minor cluster by showing just its TT sites (this time in red). At the bottom of Figure 9a, we show how these are arranged in the $NaCd_2$ unit cell. We trace out the pattern made in this packing process by using thick pink bars to connect the centers of the clusters. A look at the arrangement of the pink bars shows that each minor cluster is surrounded

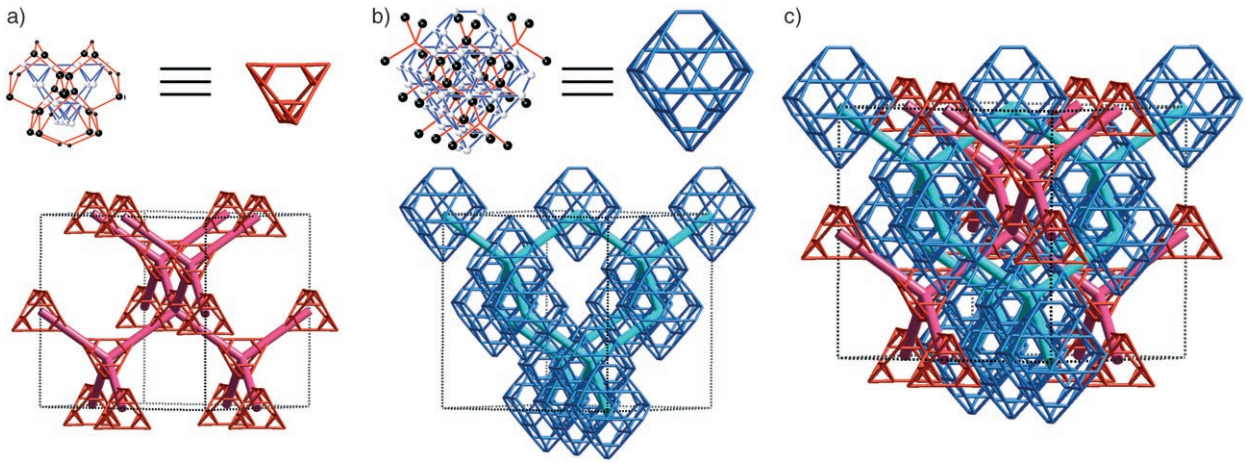

Figure 9. The packing of the minor and major clusters in the $NaCd_2$ structure. a) Packing of the minor clusters to form a diamond net (pink bars). b) The packing of the major clusters to create another diamond net (light blue bars). c) The interpenetration of these two diamond nets makes a double diamond structure of $MgCu_2$-type fragments. See this Figure animated in the Supporting Information.

tetrahedrally by four other minor clusters. Indeed, the pink bars trace out a diamond network. The minor clusters pack together in a diamondoid fashion.

In Figure 9b, we show the corresponding packing for the major cluster, drawn with a similar abbreviation. As with the minor clusters, the major clusters pack to create a diamond net (light blue bars). The diamond network of the major cluster has a different origin however: it is shifted by a translation of 0.5**c** (or equivalently, 0.5**a** or 0.5**b**) from the minor-cluster network.

The $NaCd_2$ structure results (aside from some interstitial atoms; see Section 6) from the superposition of these two diamond networks (Figure 9c). It consists of two interpenetrating diamond networks, an arrangement known as the double diamond structure. A familiar example of the double diamond structure is seen in the NaTl structure, in which the Na and Tl form separate, interpenetrating diamond networks. Another example is the cuprite, Cu_2O, structure. $NaCd_2$ is a variant on this theme: in place of the Na and Tl atoms in the NaTl structure type, it has two $MgCu_2$-type fragments of different size, the major and minor clusters.

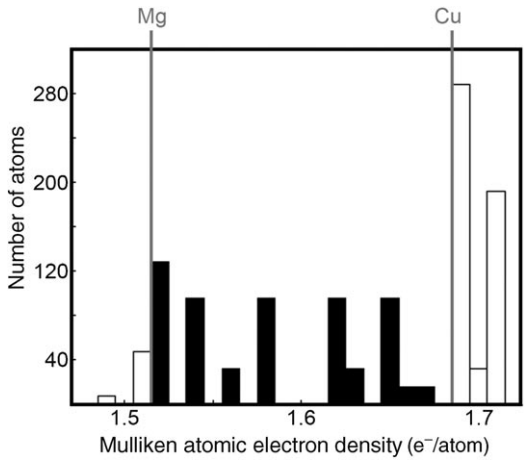

Figure 10. Histogram of the distribution of the Mulliken electron density over the atoms of the $NaCd_2$ structure. Vertical gray lines give the calculated electron density on the Mg and Cu sites of the $MgCu_2$ structure type for comparison. Black bars: sites with electron densities intermediate between the Mg and Cu lines; white bars: the remaining sites.

5. This Structure is Different: Electronically Defined Regions of Differing Polarity

Common themes can now be seen in the complex $NaCd_2$ structure and the simpler $Mg_{17}Al_{12}$ structure. Mulliken population analyses reveal both are built from packings of $MgCu_2$-type fragments. In the $Mg_{17}Al_{12}$ structure, we saw that these fragments are terminated by a layer of atoms with nonpolar electron counts. This divided the structure into regions of polar and nonpolar bonding. Let's see if such a division occurs in the more complex $NaCd_2$ structure.

In Figure 10, we plot the electron populations of the $NaCd_2$ structure as a histogram, tallying the number of atoms at each electron count. For comparison, we mark with gray lines the Mulliken populations for the Mg and Cu sites in the $MgCu_2$-type structure (at the same electron count, 1.63 electrons per atom; calculated assuming all sites were occupied with Cd atoms). If the $MgCu_2$-type fragment description fit the $NaCd_2$ structure perfectly, the histogram would consist of two sharp peaks at these electron counts. Instead, we see a spread running over the wider range of 1.49–1.71 electrons per atom. Just as in the $Mg_{17}Al_{12}$ structure, less polar sites appear with electron counts intermediate between those of the cationic and anionic sites of the $MgCu_2$ type.

In Figure 11, we illustrate in a graphic way this division between relatively polar and nonpolar sites in the structure. We take the structures of the major and minor clusters and overlay on these structures spheres which indicate the positions of the atoms in the histogram in Figure 10. The color gives the region of the histogram that atom is in. White spheres indicate that the site is either in the region of the histogram more electron-rich than the Cu sites or more electron-poor than the Mg sites in the $MgCu_2$ type. *These are*

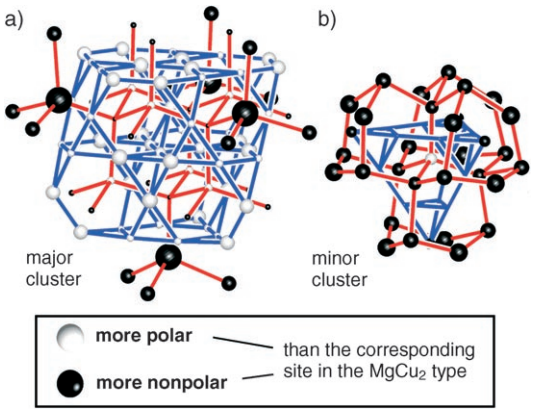

Figure 11. Polarities of the sites in a) the major cluster and b) the minor cluster of the $NaCd_2$ structure. The spheres plot the positions of the atoms of the clusters in the histogram of Figure 10. White spheres correspond to the white-bar regions of Figure 10, that is, to sites more cationic than the Mg sites or more anionic than the Cu sites in the $MgCu_2$ type. The volume of each sphere gives the site's distance in the histogram from the Mg line (for D sites) or the Cu line (for TT sites). See this Figure animated in the Supporting Information.

sites of high polarity. The atoms with black spheres lie in the mainly black-bar region intermediate between the Mg and Cu lines, *in the region of low polarity.* The volumes of the spheres are proportional to the distance of an atom from either the Mg or Cu line, the Mg line for the D sites of the $MgCu_2$-type fragments, the Cu line for the TT sites. Note that the sphere volumes here signify the difference in a site's electron density from a standard, whereas formerly they measured the electron density itself.

Qualitatively, the spheres give us a sense of how much excess charge is being piled up on each site. Sites with large white spheres approximate the cations and anions of normal ionic salt structures. Sites with large black spheres mark atoms participating in nonpolar bonding, as observed in elemental structures.

We were (and are) tempted to describe the polar regions as more ionically bonded, and the nonpolar ones as more covalently bonded. A reviewer, however, appropriately noted that we have no theoretical evidence for the bonding type other than the electron density variation, and, moreover, these charges cannot differentiate between covalent and metallic bonding.

A look at Figure 11 shows clearly that the internal portions of the clusters have greater polarities (white spheres or very small black spheres indicating polarities near that of the $MgCu_2$ type). Regions of low polarity appear at the small faces of the major cluster, on the diamondoid substructure (red in Figure 11a). The portion of the minor cluster marked by nonpolar character is greater: the small truncated-tetrahedral substructure (blue in Figure 11b), is completely enveloped by a shell of black spheres.

As in the $Mg_{17}Al_{12}$ structure, the polar and nonpolar sites of the $NaCd_2$ structure are segregated between the interior and exterior of the structure's component $MgCu_2$-type fragments. Recall in the former structure that there are sites at the interfaces between neighboring clusters which can either be viewed as belonging to the electron-poor network of one cluster or the electron-rich network of the neighboring cluster: such dual sites thus acquire an intermediate, less polar, character. Does a similar geometrical factor come into play in the more complex $NaCd_2$ structure? To answer this, we turn to the geometry of the interfaces between $MgCu_2$-type fragments in $NaCd_2$.

6. Interfaces in the $NaCd_2$ Structure

6.1. Mac and Mic

An easy way to visualize the interfaces between the $MgCu_2$-type fragments in the $NaCd_2$ structure is to look at the positions of the interstitial atoms—atoms not uniquely assignable to any one $MgCu_2$-type fragment—of the structure (112 of the 1192 atoms per unit cell). They consist of two symmetry-distinct sites. The first set of sites, Cd2, is overlaid on the $NaCd_2$ unit cell in Figure 12a. The sites trace out

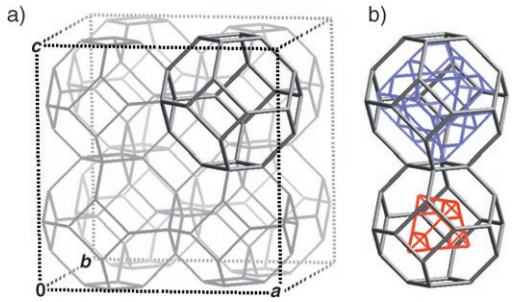

Figure 12. Interfacial planes between $MgCu_2$-type fragments in the $NaCd_2$ structure. a) One of the interstitial sites, Cd2, traces out space-filling truncated octahedra joined by face sharing (gray). b) The cavities of the truncated octahedra are occupied by $MgCu_2$-type fragments. Blue: the major cluster; red: the minor cluster. The faces of the truncated octahedra lie on the interfacial planes separating the $MgCu_2$-type fragments. See Figure 9 for structural abbreviations. See this Figure animated in the Supporting Information.

truncated octahedra. These share faces to fill space, dividing it into large cavities. Each cavity is then occupied by a $MgCu_2$-type fragment (Figure 12b). The faces shared by the truncated octahedra delineate the interfaces between the $MgCu_2$-type fragments. Four types of interfaces arise: major cluster–major cluster (MaC–MaC), minor cluster–minor cluster (MiC–MiC), and two types of major cluster–minor cluster (MaC–MiC) interfaces. The MiC–MiC interfaces are comparatively small—reflecting the clusters' small size. We'll focus on the interfaces involving at least one major cluster.

We show these interfaces in Figure 13, where we construct the nearest-neighbor clusters around a single major cluster. There are four nearest-neighbor major clusters, joining the central cluster at every other hexagonal face. This creates a tetrahedron of major clusters around the central cluster (Figure 13a). The remaining hexagonal faces of the truncated octahedron are capped with minor clusters, to create a tetrahedron of minor clusters (Figure 13b). Together the tetrahedra of major and minor clusters comprise a "cube" of $MgCu_2$-type fragments around the central major cluster. Additional minor clusters occur across the rectangular faces

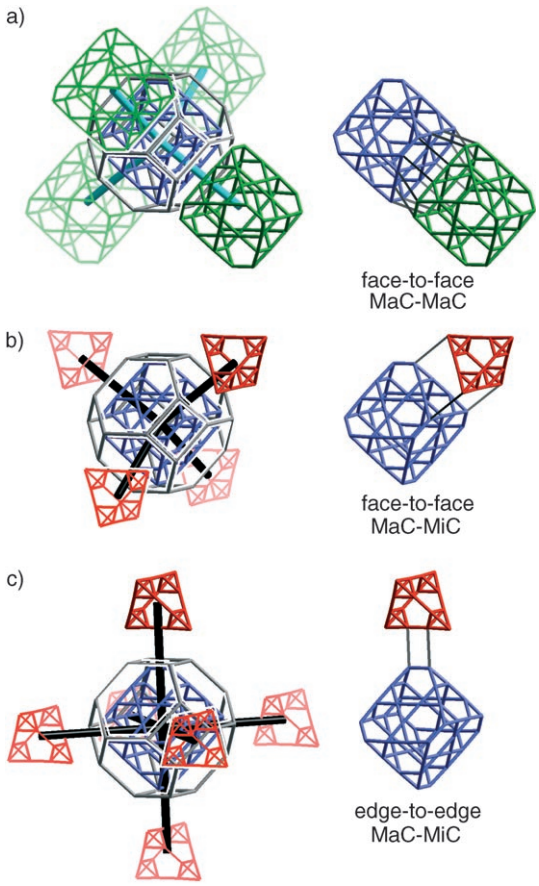

Figure 13. A schematic view of the interfaces of each major cluster with its neighboring clusters in the $NaCd_2$ structure using the abbreviations introduced in Figure 9. a) The neighboring major clusters (green) are arrayed in a tetrahedral fashion about the central major cluster (blue). b) One set of neighboring minor clusters (red) is arranged in a tetrahedron around the major cluster. c) A second set of neighboring minor clusters is arranged around the central major cluster to form an octahedron. At the right of (a)–(c), we show how each type of neighbor is joined to the major cluster. In (a) and (b), the intercluster interfaces occur between faces of the clusters. In (c), the interface is smaller, occurring between edges of the clusters. We will refer to these interfaces as the (a) face-to-face MaC–MaC, (b) face-to-face MaC–MiC, and (c) edge-to-edge MaC–MiC interfaces. More detailed views of these interfaces will be given in Figures 14–17. See this Figure animated in the Supporting Information.

of the truncated octahedron, making up an octahedron (Figure 13c).

Altogether, each major cluster is neighbored by a 4 + 4 + 6 arrangement of clusters. These three types of neighbors correspond to the three types of interfaces shown on the right panels of Figure 13a–c and are listed in Table 3: the face-to-face MaC–MaC, face-to-face MaC–MiC, and edge-to-edge MaC–MiC interfaces, respectively.

Table 3: Interfaces between $MgCu_2$-type fragments in the $NaCd_2$ structure.

Interface	Structure type	Bonding character
face-to-face MaC–MaC	$MgZn_2$	polar[a]
face-to-face MaC–MiC	Al_3Zr_4	nonpolar
edge-to-edge MaC–MiC	Al_3Zr_4	nonpolar

[a] Slightly less polar than the $MgCu_2$-type fragments.

The interfaces between clusters in the $NaCd_2$ structure are not just a way of accounting for stragglers in the structure. We will show that the interface regions are structurally distinct, themselves pieces of known structure types (second column in Table 3). And, more importantly perhaps, each interface has electronic characteristics (third column) that mediate and link the polar or nonpolar nature of bonding within the clusters.

6.2. The Face-to-Face MaC–MaC Interface: One Laves Phase Separates Touching Clusters of Another

A closer look at the contacts between these clusters reveals a regularity in their packing. Take the MaC–MaC contact (Figure 14). The major clusters are separated by a hexagonal face of interstitial atoms from the truncated-octahedral net (gray spheres) with another interstitial atom at the center of the hexagon. Across this hexagon, the two major clusters face each other via the larger of their two types of faces.

In Figure 14b and c, we show how the two major clusters are connected with each other across the interface. The truncated-tetrahedral networks (top) are bridged via the interstitial atoms, as indicated with dotted lines in Figure 14b. In Figure 14c, we redraw these with dark rods. They continue the labyrinth of hexagons and triangles of the original truncated-tetrahedral frameworks. Indeed, these new contacts trace out additional truncated tetrahedra.

Something similar happens between the diamondoid nets (bottom of Figure 14b,c). The terminal atoms of the two diamondoid fragments meet so as to mutually extend their tetrahedral coordination. In this way the diamondoid network is continued across the interface. Note that these new linkages create six-membered rings in the boat conformation, while in the $MgCu_2$ structure type the diamondoid net is built exclusively of chairs. The presence of boats is indicative of the hexagonal diamond structure. Indeed, the interface forms the center of a large fragment of the hexagonal diamond structure; we highlight this fragment in green at the bottom of Figure 14c.

The two major clusters thus join to form truncated tetrahedra and a fragment of the hexagonal diamond structure. These are highlighted with green in Figure 14c. These two frameworks interpenetrate each other to form a fragment of the hexagonal Laves phase, the $MgZn_2$ structure type. This $MgZn_2$-type linkage occurs at each of the four large faces of a major cluster.

Note that at the MaC–MaC interface the diamondoid network of one major cluster joins continuously with the diamondoid network of the neighboring major cluster. No scrambling of D and TT sites occurs at this interface. As expected, polarity plots of these interfaces (not shown) show that the polar character of the diamondoid networks passes largely without interruption across the interface, in contrast to the other interfaces in the structure.

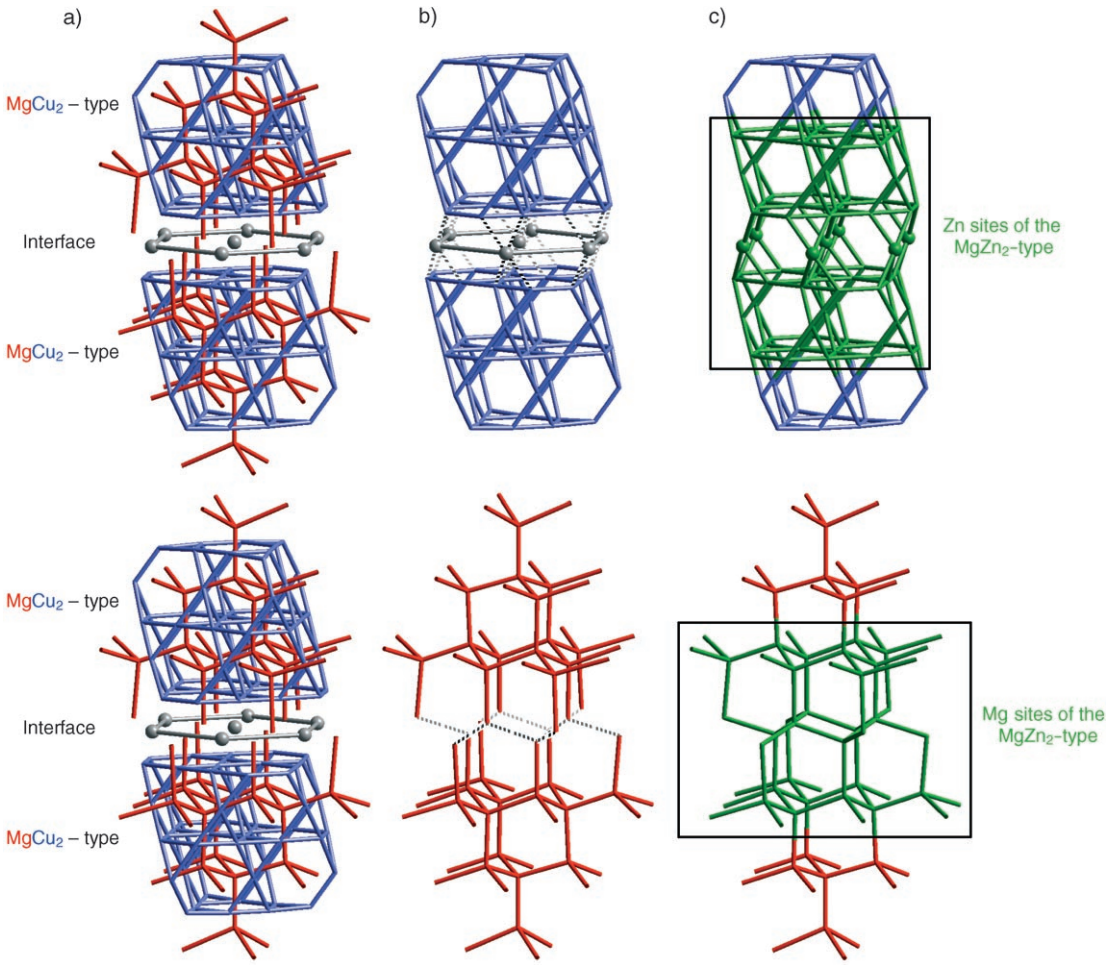

Figure 14. The face-to-face MaC–MaC interface in the $NaCd_2$ structure. a) Two major clusters face each other across a layer of interstitial atoms (gray spheres). b) The truncated-tetrahedral (top) and diamondoid (bottom) frameworks of the two major clusters drawn separately. The dotted lines show the continuation of these connectivity patterns across the interface. c) The truncated-tetrahedral (top) and diamondoid (bottom) networks incorporating these intercluster connections. In green are highlighted the portions of these two networks which match, respectively, the Zn and Mg sites of the $MgZn_2$ structure type. See this Figure animated in the Supporting Information.

6.3. Al_3Zr_4-Type Layers at the MaC–MiC Interfaces

In Figure 13b, we showed what happens at the remaining hexagonal faces of the truncated octahedra around the major clusters. Through these faces, the major cluster (blue) is linked to four minor clusters (red). At each of these interfaces, the smaller faces of the major cluster meet one of the triangular faces of a minor cluster to make a very large trigonal prism (at right in Figure 13b).

If we zoom in on this interface, we can see that a simple structure type is also being formed here. We illustrate this in Figure 15 (note that the clusters have been reoriented from Figure 13b). First, in Figure 15a, we show the two clusters separately, the major cluster on top, the minor cluster on bottom. Then, in Figure 15b and c, we trace how the atoms of the clusters come together at the interface. In particular, we emphasize ten key atoms on the diamondoid networks of the two clusters, drawing them as yellow and purple spheres. These form two tetrahedra which point into the interface with their triangular bases (purple spheres).

As we bring the clusters together (Figure 15b), these triangular atoms interdigitate to form a hexagon. This is traced out in Figure 15c. In the process, the atoms drawn in yellow join to make a linear chain passing through this hexagon and through the hexagonal faces of the truncated-tetrahedral nets of the major and minor clusters. The result: a distorted hexagon (purple) sandwiched by two kagomé-net fragments (blue) and skewered by a linear chain (yellow).

Are these structural features new? No, they actually are there in a simple, but rather rare, intermetallic structure type, the Al_3Zr_4 type. In this structure (Figure 15d), kagomé nets of Al atoms alternate with graphitic layers of Zr atoms to make hexagonal channels. These channels are then occupied by linear Zr chains. The Al_3Zr_4 framework at this interface actually extends further than the small segment we've shown in Figure 15c, incorporating atoms both from the truncated-octahedral net and more atoms from the diamondoid nets.

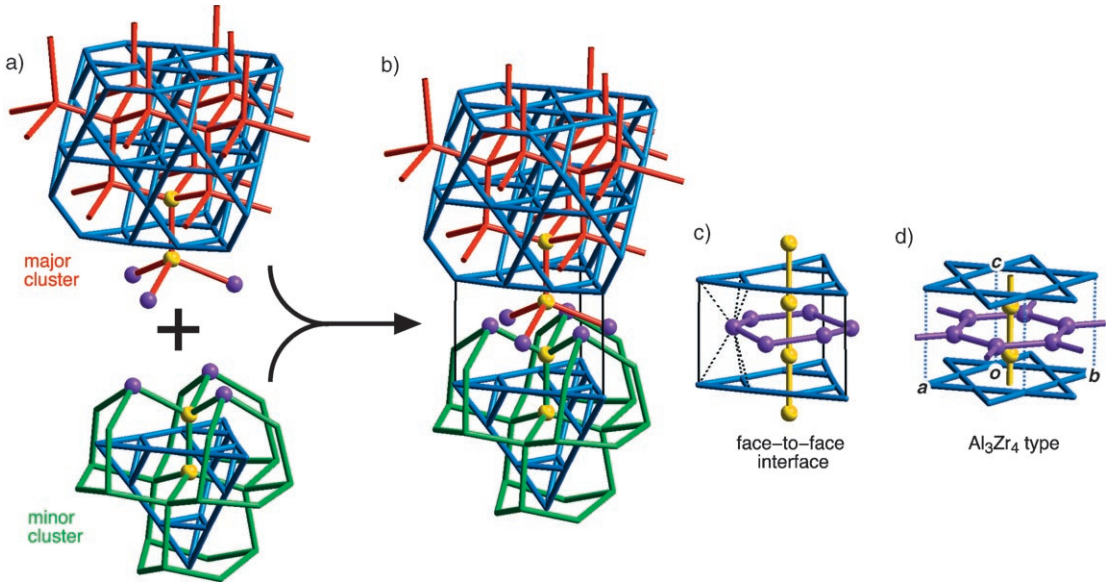

Figure 15. The face-to-face major cluster–minor cluster (MaC–MiC) interface in the $NaCd_2$ structure. a) The major and minor clusters viewed separately, and then b) viewed together. c) The interface atoms between these two clusters form a distorted fragment of the Al_3Zr_4 structure type. d) The Al_3Zr_4 structure type. Al blue, Zr yellow and purple. In (a) and (b), we trace the source of the Zr sites at the face-to-face Al_3Zr_4-type interface in (c) from the major and minor clusters by overlaying yellow and purple spheres on the corresponding sites in the major and minor clusters. See this Figure animated in the Supporting Information.

6.4. MaC–MiC Interfaces as Nonpolar Regions

It is at this shift from regions of $MgCu_2$-type to Al_3Zr_4-type features that we start to see regions of nonpolarity. In Figure 16, we redraw the formation of this Al_3Zr_4-type interface, this time plotting their polarities. We again start with the major and minor clusters coming together at this interface, with their diamondoid nets interdigitating (Figure 16a). In the process of interdigitating, the two clusters create a slab of black spheres. As we pass across the interface from the major cluster to the minor cluster, we pass through a several-atom-thick layer of black spheres.

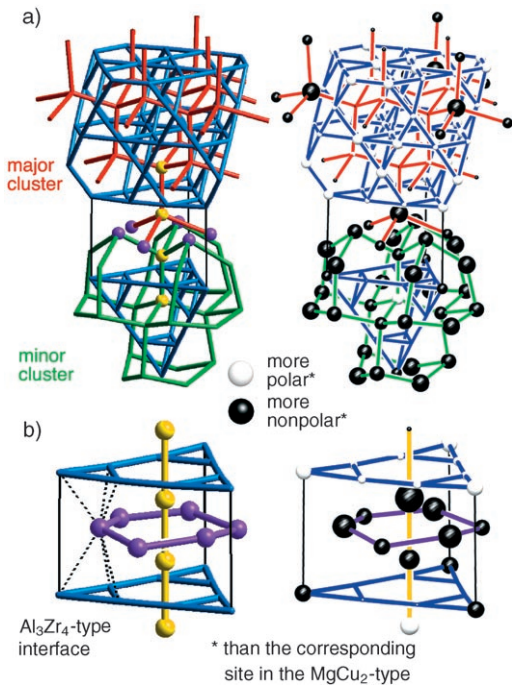

Figure 16. The site polarities at the face-to-face MaC–MiC interface. a) The major and minor clusters joining at the face-to-face interface. b) A close-up of the Al_3Zr_4-type face-to-face interface (Al-type sites: blue, Zr-type sites: yellow and purple). Note that all the Zr-type sites between the two kagomé layers drawn in blue all show low polarity. The caption to Figure 11 gives the conventions on the plotting of the site polarity. See this Figure animated in the Supporting Information.

Similar results are also seen at the other type of MaC–MiC interface, the edge-to-edge MaC–MiC interface (not shown): a small fragment of the Al_3Zr_4 structure type links the clusters across a rectangular face of the truncated-octahedral net. The sites of this fragment are dominated by nonpolarity. This nonpolar character is largely restricted to the diamond networks of the major and minor clusters.

From this analysis of the interfaces in the $NaCd_2$ structure, we see that the interfaces between the $MgCu_2$-type fragments themselves form regions of simple structure types. These are summarized in Table 3.

7. Productive Ambiguity: Creating Nonpolar Interfaces by Cluster Packing

We saw that the minor and major clusters join at interfaces to generate thin regions of the Al_3Zr_4 structure type, and that the diamondoid network sites at the interfaces are unusually nonpolar in their bonding. Why do these D sites show this nonpolarity? Following our results on the $Mg_{17}Al_{12}$ structure (see Section 2), we believe the explanation is in a structural ambiguity in these interface regions—they can be thought of as belonging to oppositely polarized networks, the electron-poor diamondoid networks and the electron-rich truncated-tetrahedral networks.

Perhaps we can make this geometrically difficult yet crucial point clearer by taking a second look at the simpler of the two Al_3Zr_4-type interfaces, the face-to-face MaC–MiC interface discussed in Section 6.3, shown again in Figure 17a.

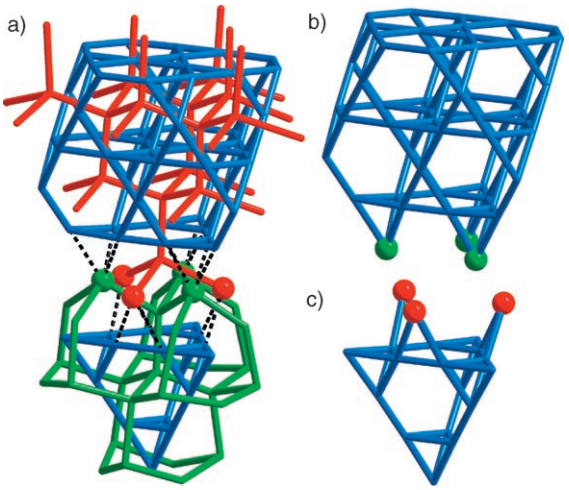

Figure 17. The extension of the major and minor clusters into the face-to-face MaC–MiC interface in the $NaCd_2$ structure. a) The major and minor clusters meeting at the interface. b) The extension of the major cluster truncated-tetrahedral network through the incorporation of D sites (green spheres) from the minor cluster. c) The complementary extension of the minor cluster truncated-tetrahedral net by including D sites (red spheres) from the major cluster. See this Figure animated in the Supporting Information.

As the diamondoid networks of the two fragments interdigitate, the outermost D sites of one cluster come in close contact with the TT sites (blue) of the neighboring cluster. We draw out these contacts with dotted lines. In Figure 17b and c, we focus in on these contacts for the major and minor clusters separately. As can be seen from the Figure, the kagomé-net patterns of the truncated-tetrahedral networks are continued by these intercluster contacts to D sites; the external D sites of one cluster augment the truncated-tetrahedral network of the other.

The ambiguity in the network allegiance of these sites is reflected in their electron populations: whereas the TT and D sites are respectively electron-rich and electron-poor, these interface sites exhibit intermediate electron populations.

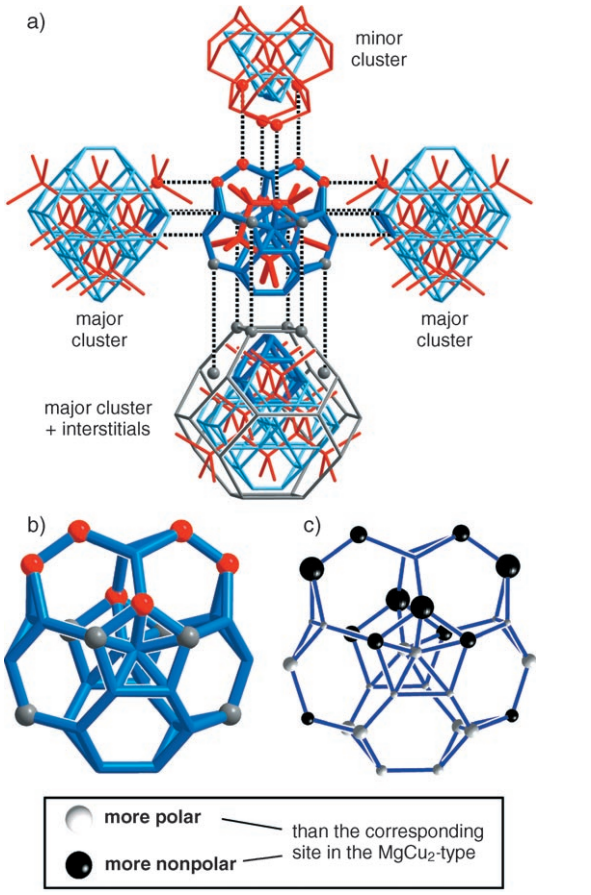

Figure 18. The construction of Samson's pentagonal cluster of Friauf polyhedra from Andersson's $MgCu_2$-type clusters. a) Samson's cluster, with the its overlapping $MgCu_2$-type clusters drawn separately. Every atom of the pentagonal cluster has its origin in one of these $MgCu_2$-type clusters or their associated interstitial atoms. Black dotted lines show this mapping of sites between the $MgCu_2$-type cluster and the pentagonal cluster. b) The truncated-tetrahedral part of Samson's cluster. c) Polarity plot for the truncated-tetrahedral portion of the pentagonal cluster. Blue bars: TT sites on the major or minor clusters; red bars and spheres: D sites on the major or minor clusters; gray spheres: interstitial sites. The polarity of these sites follows their origin in the $MgCu_2$-type fragment scheme; the more nonpolar sites are TT sites on the pentagonal cluster, but D sites or interstitial sites on the $MgCu_2$-type clusters. The caption to Figure 11 gives the conventions on plotting of site polarities. See this Figure animated in the Supporting Information.

8. Samson's Pentagonal Clusters from $MgCu_2$-Type Fragments

So far our Aufbau has focused on the $MgCu_2$-type fragments in the $NaCd_2$ structure. Can we make a link to Samson's picture? Or, to put it another way, how does Samson's pentagon of Friauf polyhedra arise from Andersson's $MgCu_2$-type clusters? The easiest way to see this is to first draw Samson's pentagon and then draw the $MgCu_2$-type clusters that contribute to it, separately while tracing the correspondences. We show this in Figure 18a, where we draw the pentagonal cluster at the center, with the $MgCu_2$-type clusters drawn off N, E, S, W of the Figure. We highlight the atoms they contribute to Samson's cluster with thick bars and spheres, and trace the correspondences with dotted lines. Four $MgCu_2$-type clusters (three major, one minor), along with some interstitial atoms, are involved. They meet at the pentagonal cluster in a cross-shaped geometry.

Note that in the formation of the cluster, some sites are taken from the diamondoid (electron-poor) networks of the $MgCu_2$-type clusters to build the truncated-tetrahedral (electron-rich) part of the pentagon of Friauf polyhedra. Figure 18b focuses on this, showing just the truncated-tetrahedral component of the cluster. The sites are color-coded according to their origins in the $MgCu_2$-type fragment

scheme: blue bars for TT sites (analogous to the Cu sites of $MgCu_2$); red spheres for D sites (analogous to the Mg sites of $MgCu_2$); gray spheres for interstitial sites.

In Figure 18c, we compare this with the site polarities (calculated using the assignments in the $MgCu_2$-type fragment scheme). *Samson's pentagon of truncated-tetrahedral clusters consists of both polar and nonpolar sites.* The identification of these sites follows their origins in Andersson's fragments. The polar sites are truncated-tetrahedral in Andersson's view, as they are here in Samson's construction. The nonpolar sites, on the other hand, are diamondoid or interstitial in Andersson's view, in contrast to Samson's perspective where they are truncated-tetrahedral.

We come to the following Aufbau for the $NaCd_2$ structure: start with the $MgCu_2$ structure type, break it up into small $MgCu_2$-type fragments, and fuse them back together. The polarity of the substructures is a guide to further assembly, with interesting things happening at the interfaces. Samson's pentagonal clusters of Friauf polyhedra emerge only at this late stage. Interestingly, they connect atoms of very different bonding type.

9. Interpenetrating Regions of Polar and Nonpolar Bonding

We have made an argument that in these complex phases, in clearly metallic materials, at the microscopic level one finds not just a partitioning into clusters, but—much more interestingly—a partitioning of the lattice into regions of polar and nonpolar bonding. We know these categorizations are exaggerations, if not caricatures. But let's look for connections as far afield as we can, because nature is trying to tell us something.

The first connection we see is to a group of other materials with polar and nonpolar regions interpenetrating, the "Swiss-cheese metals" of the alkali-metal suboxide class.[72] In these, for instance Rb_9O_2,[73] one has regions of metallic alkali-metal bonding surrounding islands of polar bonding. Nanocomposites of metallic RuO_2 and hydrated surface proton-conducting domains also combine regions of differing conductivity.[74]

The second connection we would like to make is to the burgeoning field of elemental structures under high pressure.[75–78] Most of the heavier main-group elements (including examples from every Group, from the alkali metals to the halogens) depart under very high pressure from the normal close-packed structure for structures of lower symmetry. Which, nevertheless, are denser. Consider, for instance, Ba at 12.6 GPa;[79] it goes into a host–guest structure, with Ba atoms forming both channels and the occupants of these channels. The complexity doesn't end here: these host and guest substructures are incommensurate with respect to each other.

How is one to make sense of these structures? Well, one way is to think that they consist of two interpenetrating sublattices, within which the atoms of the same element are bonded to each other in different ways, exploring varieties of electron transfer and electron correlation. Atoms (networks) of different size can pack more efficiently than identical atoms. We think that some of these high-pressure phases may have in them sublattices of polar and nonpolar bonding.

The most interesting connection that suggests itself is to minimal surfaces[80–85] and the geometrics of diblock copolymers.[86,87] In the latter, a duality in the building blocks, A–B, translates (with the aid of small intermolecular forces) into a variety of beautiful structural types, sometimes ordering the sub-blocks along minimal surfaces.

We feel that something of this kind is at work in these complex intermetallic phases, with the regions of polar and nonpolar bonding taking the role of A and B. Andersson's group already made the first of these connections, noticing that Riemann's D surface can be used to divide the $NaCd_2$ structure into two distinct parts.[46] A further, quantum-mechanically motivated connection to these A–B phases is seen in the separate networks formed by the major and minor clusters. We saw in Figure 9 that the major clusters are arranged at the vertices of a diamond network that is interpenetrated by another diamond network formed by the minor clusters. Taken together, the major and minor clusters then trace out the double diamond structure. In the double diamond structure, the interface between the two individual diamond networks marks out the D surface. So, we can imagine that the volumes occupied by the major clusters and minor clusters can be divided by this surface.

But how would such a division relate to the bonding in $NaCd_2$? A look at the polarity plots for the major and minor clusters (Figure 11) indicates that, on the whole, a different kind of bonding is prevalent in each. The minor cluster is essentially dominated by nonpolar sites (large black spheres), while in the major cluster, polar character is more pronounced. The major-cluster and minor-cluster regions then correspond to regions of, respectively, polar and nonpolar character.

In Figure 19, we show this division by overlaying the D surface on the $NaCd_2$ unit cell and plotting the site polarities in our usual way, with black and white spheres, black for nonpolar, white for polar. The two sides of the surface are drawn in blue and green. The blue side faces the major clusters, the green the minor clusters. The polarities for the sites within the blue region are plotted in Figure 19a. While some exceptions occur, this region is occupied chiefly by white spheres, indicating polar bonding. The situation is quite different for the other side of the surface (Figure 19b). Here, large black spheres dominate, reflecting nonpolar bonding in this region. *In the $NaCd_2$ structure, regions of different bonding character (polar and nonpolar) are separated by the D surface.* This segregation seems analogous to that found in hydrophobic–hydrophilic and other A–B systems.

What is the driving force for this segregation? One possibility is that the nonpolar regions serve as an electron sink or source to tune the electron counts (and through them the bonding) of the more polar $MgCu_2$-type fragments. And of the nonpolar regions as well. Indeed, a small degree of electron transfer occurs between the two sides of the D surface: the sites on the polar (blue) side of the surface are more electron-rich on average by 0.02 electrons per atom, with the sites on the nonpolar (green) side being electron-poor by 0.02 electrons per atom.

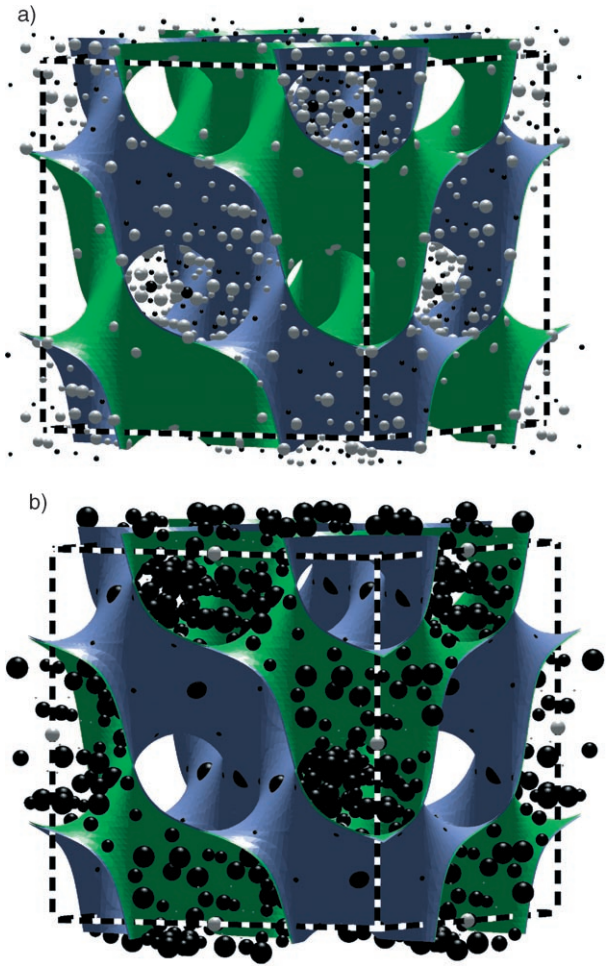

Figure 19. Division of the polar and nonpolar regions in the $NaCd_2$ structure by the D surface. The D surface is overlaid on the $NaCd_2$ unit cell with the two sides of the surface drawn in blue and green. The $NaCd_2$ site polarities are plotted a) for the volume bound by the blue side of the surface and b) for the green side. The caption to Figure 11 gives the conventions on plotting of site polarities. See this Figure animated in the Supporting Information.

10. The Aufbau Suggests Other Structures

Perceiving that the $NaCd_2$ structure is built from $MgCu_2$-type blocks suggests the possibility of a series of structures based on variously sized fragments of the $MgCu_2$ structure type, or other Laves phase structure types. Many examples are already known, for instance the α-Mn structure, in which the $MgCu_2$ structure type is truncated down to a single Friauf polyhedron. Further examples are the rhombohedral $Zr_{21}Re_{25}$[88] and μ-W_7Fe_6 structures, which consist of, respectively, columns and layers of Laves phase structure types.

Hints of the further growth of the $MgCu_2$-type clusters beyond those found in the $NaCd_2$ structure are also present in the Mg_2Al_3 structure. In this structure, the region corresponding to the minor cluster in $NaCd_2$ is severely disordered, but we can perceive patterns within the disorder. For instance, in Figure 20, we show one element in this disorder: the growth of the major cluster along its small faces into the minor cluster

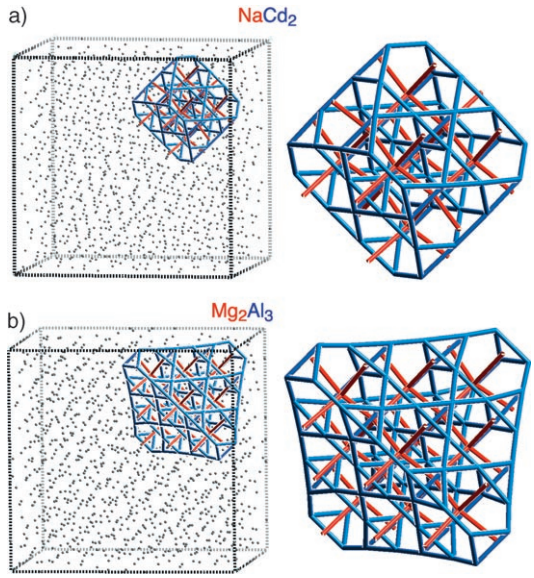

Figure 20. The expansion of the major cluster in the Mg_2Al_3 structure. a) The unit cell (left) and one of the major clusters (right) of the $NaCd_2$ structure. b) The unit cell (left) and one of the expanded major clusters (right) of the Mg_2Al_3 structure (idealized; see text). See this Figure animated in the Supporting Information.

regions, such that the major cluster takes on a tetrahedral rather than octahedral appearance. This expanded major cluster (the Big MaC of $MgCu_2$-type fragments) is disordered with the original minor cluster and additional sites, indicating the facile way in which the $MgCu_2$-type fragments can feed off of each other.

11. Conclusions

For more than 40 years now, the $NaCd_2$ structure and its structural relatives, Mg_2Al_3 and Cu_4Cd_3, have been objects of intense aesthetic contemplation by pattern hunters and geometers of nature. Have we succumbed to the same obsession? Perhaps, yet we think we have come a bit further: we have used a touch of quantum mechanics to probe how these structural schemes are connected with the underlying bonding.

The Mulliken electron populations point the way to a coarse division of the sites into electron-rich and electron-poor. This first, rough division in $NaCd_2$ reveals two different blocks of the $MgCu_2$ structure type, the major cluster and minor cluster. The electron-rich sites lie on the Cu sites of the $MgCu_2$-type fragments, with the sites interconnecting to form truncated tetrahedra. The electron-poor sites lie on the Mg sites of the $MgCu_2$-type fragments, which interconnect to form diamondoid networks. This picture of the structure converges, geometrically, with the remarkable description of the structure by Andersson and co-workers in 1987.[46]

But the story does not end with a description of interpenetrating polar cluster networks. The regions between the form-giving clusters emerge as regions of nonpolarity. Their

polarity is reduced by a geometrical ambivalence at the cluster periphery that parlays into relative nonpolarity: the external D sites of the fragments may be joined (conceptually) with the sites of neighboring clusters either to augment the truncated-tetrahedral networks of the neighboring clusters or to generate new truncated tetrahedra. These nascent truncated tetrahedra nucleate pentagonal clusters of Friauf polyhedra, the keystone of Samson's original description of this structure, as well as several of his other magnificent structures.

Thus, an electronic Aufbau of $NaCd_2$ leads naturally to a kind of structural complementarity, blending Samson's and Andersson's perspectives, even as the latter follows more clearly the electronic imperatives. Indeed, it is unlikely that structures of this complexity could be pinned down by any one construction. The manifold ways this structure has been described actually reflect their underlying electronics, the remarkable way in which polar and nonpolar substructures interpenetrate and interact.

Appendix

Electronic-Structure Calculations on $Mg_{17}Al_{12}$

We calculated Mulliken populations for the $Mg_{17}Al_{12}$ structure with the extended Hückel (eH) method, making all atoms Al. The eH parameters were calibrated against LDA-DFT calculations with the VASP package.[89–92] First the unit-cell volume was optimized using a $5\times5\times5$ k-point mesh generated with the Monkhorst–Pack scheme.[93] The charge density and the potential were then calculated using a $12\times12\times12$ k-point mesh. Using this charge density and potential, the band structure of Figure 21 a was calculated k-point by k-point. The ultrasoft Vanderbilt pseudopotentials[94] provided with the package were used throughout. In each calculation, eigenstates for 75 bands were calculated using plane-wave basis sets in the high-precision mode. This corresponds to an energy cutoff of 161.5 eV.

We then compared this LDA-DFT band structure to an eH band structure calculated with the YAeHMOP package.[95] In our initial eH calculation, all atoms were made Al and the default eH parameters were used, and the cell constants were taken from the LDA-DFT optimization. The resulting band structure showed some correspondences with the LDA-DFT band structure, for instance, the wide opening at the Fermi energy (E_F) at H. However, the dispersion of the bands near the E_F appeared exaggerated. To correct this, the ζ(3s) and ζ(3p) exponents, which measure the sharpness of the exponential decay of the orbitals, were changed from 1.167 to 1.267. The Al parameters were then $H_{ii}(3s) = -12.5$ eV, $H_{ii}(3p) = -6.5$ eV, $\zeta(3s) = 1.267$, and $\zeta(3p) = 1.267$. The band structure calculated using these parameters is compared with the LDA-DFT band structure in Figure 21. While some differences can be seen between the two band structures, the qualitative similarity is striking, considering that the eH band structure was calculated on an model which ignores that the structure is built from both Al *and* Mg atoms, while the LDA-DFT calculation was made using the experimentally determined ordering of Al and Mg atoms.

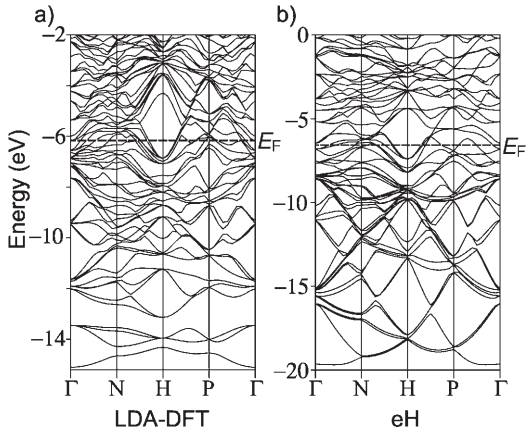

Figure 21. Band structures of the $Mg_{17}Al_{12}$ structure. a) The LDA-DFT band structure. b) The eH band structure for an elemental model of the $Mg_{17}Al_{12}$ structure in which all sites are assumed to be Al. The dashed lines give the Fermi energy (E_F) for each band structure. $\Gamma = (0,0,0)$, $N = (0,0,1/2)$, $H = (1/2,-1/2,-1/2)$, $P = (1/4,1/4,1/4)$.

Atomic Coordinates for $NaCd_2$

Two structure solutions exist for the $NaCd_2$ structure: Samson's original solution (1962)[32] and Andersson's group's redetermination (1987).[46] The two structure solutions differ in two respects. First, for the 17 symmetry-distinct sites, the positions differ by up to 0.23–0.25 Å (for some of the D sites of the major cluster). Second, the two solutions differ in the degree of mixed occupancies and partial occupancies (see Section 4.2). We have performed eH calculations on both structures and have found similar results. The calculations we report here use the structural positions from Andersson's structure.

In this model, many of the sites have mixed occupancy, but in each case the Na and Cd occupations add up to 1; that is, the sites are fully occupied, but it's variable whether the atoms there are Na or Cd. There is one site in this model, Cd9, which exhibits a fractional occupancy of 0.5. This site is on the truncated-tetrahedral network of the minor cluster (see Figure 8). Full occupation of this site would lead to short Cd9–Cd9 contacts of 2.30 Å between neighboring minor clusters, drastically smaller than the 2.96 Å typical of Cd–Cd contacts in this structure. In our calculations, we resolved this problem by making the Cd9 sites on one of the two minor clusters in the primitive unit cell fully occupied, and leaving the Cd9 sites on the other minor cluster fully vacant. This ordering reduces the symmetry of the $NaCd_2$ structure from $Fd\bar{3}m$ to $F\bar{4}3m$, in which there are two symmetry-distinct major and minor clusters in the unit cell. We used the charge calculated for the occupied Cd9 site for all the Cd9 sites in the structure. For the remaining sites, we averaged the charges to regain the full $Fd\bar{3}m$ symmetry.

Elemental Model for $NaCd_2$

We performed eH calculations on the resulting structure, making all atoms Cd. The electron count was set to 1.63 electrons per atom to match Andersson's refined composition, $Na_{1.11}Cd_{1.89}$. The calculations were made with the YAeHMOP package,[95] using YAeHMOP's default Cd parameters: $H_{ii}(5s) = -11.8$ eV, $H_{ii}(5p) = -8.2$ eV, $\zeta(5s) = 1.64$, $\zeta(5p) = 1.60$. We previously demonstrated that these Cd parameters reproduce well the LDA-DFT band structure of the cubic γ-brass structure,[96] which, similarly to $NaCd_2$, consists of $MgCu_2$-type fragments and has an ideal electron count near that of $NaCd_2$ (21/13 = 1.62 electrons per atom for γ-brass vs. 1.63 electrons per atom for $Na_{1.11}Cd_{1.89}$).

We are grateful for the financial support of the National Science Foundation (through grants DMR-007358 and DMR-0504703) and the Petroleum Research Fund. We thank Prof. Sven Lidin for engaging discussions on the Samson structures and his comments on this paper, Jeppe Christensen for discussions on the Mg_2Al_3 structure, Prof. Veit Elser for his insights into the connection between these phases and quasicrystals, and the three reviewers of this paper. We also thank Dr. Joshua Teal Schmidt and Dr. Yongkwan Dong for discussions on the related phases they have synthesized, and Dr. Junliang Sun for sharing his calculations on the Laves phases. D.C.F. thanks Prof. Lidin for his warm welcome at Stockholm University, where the final draft of this paper was completed, and the National Science Foundation for financial support during his stay at Stockholm University through a postdoctoral research fellowship (DMR-0502582).

Received: April 28, 2006
Published online: February 8, 2007

[1] M. Hansen, *Constitution of Binary Alloys*, *2nd ed.*, McGraw-Hill, New York, **1958**.
[2] F. Laves, K. Lohberg, P. Rahlfs, *Nachr. Ges. Wiss. Goettingen Math.-Phys. Kl. Fachgruppe II* **1934**, *1*, 67.
[3] S. Samson, E. K. Gordon, *Acta Crystallogr. Sect. B* **1968**, *24*, 1004.
[4] S. Samson, *Acta Crystallogr.* **1965**, *19*, 401.
[5] D. P. Shoemaker, R. E. Marsh, F. J. Ewing, L. Pauling, *Acta Crystallogr.* **1952**, *5*, 637.
[6] G. Bergman, J. L. T. Waugh, L. Pauling, *Acta Crystallogr.* **1957**, *10*, 254.
[7] P. B. Belbéoch, H. Frisby, M. Roulliay, *Acta Crystallogr. Sect. B* **1974**, *30*, 2784.
[8] L. Arnberg, A. Jonsson, S. Westman, *Acta Chem. Scand. Ser. A* **1976**, *30*, 187.
[9] M. L. Fornasini, B. Chabot, E. Parthé, *Acta Crystallogr. Sect. B* **1978**, *34*, 2093.
[10] A. S. Koster, J. C. Schoone, *Acta Crystallogr. Sect. B* **1981**, *37*, 1905.
[11] V. K. Pecharskii, O. I. Bodak, V. K. Bel'skii, P. K. Starodub, I. R. Mokra, E. I. Gladyshevskii, *Kristallografiya* **1987**, *32*, 334.
[12] D. P. Shoemaker, C. B. Shoemaker in *Introduction to Quasicrystals: Aperiodicity and Order*, *Vol. 1* (Ed.: M. V. Jarić), Academic Press, Boston, **1988**, pp. 1–57.
[13] S. Lidin, M. Jacob, A. K. Larsson, *Acta Crystallogr. Sect. C* **1994**, *50*, 340.
[14] S. Mahne, B. Harbrecht, *J. Alloys Compd.* **1994**, *203*, 271.
[15] G. Kreiner, M. Schäpers, *J. Alloys Compd.* **1997**, *261*, 83.
[16] A. V. Morozkin, Y. D. Seropegin, V. K. Portnoy, I. A. Sviridov, A. V. Leonov, *Mater. Res. Bull.* **1998**, *33*, 903.
[17] Z. M. Mo, H. Y. Zhou, K. H. Kuo, *Acta Crystallogr. Sect. B* **2000**, *56*, 392.
[18] P. Salamakha, O. Sologub, G. Bocelli, S. Otani, T. Takabatake, *J. Alloys Compd.* **2001**, *314*, 177.
[19] C. P. Gómez, S. Lidin, *Chem. Eur. J.* **2004**, *10*, 3279.
[20] W. Hornfeck, S. Thimmaiah, S. Lee, B. Harbrecht, *Chem. Eur. J.* **2004**, *10*, 4616.
[21] V. Elser, C. L. Henley, *Phys. Rev. Lett.* **1985**, *55*, 2883.
[22] W. Steurer, *Mater. Res. Soc. Symp. Proc.* **2001**, *643*, K3.2.1.
[23] F. C. Frank, J. S. Kasper, *Acta Crystallogr.* **1958**, *11*, 184.
[24] F. C. Frank, J. S. Kasper, *Acta Crystallogr.* **1959**, *12*, 483.
[25] A. J. Bradley, P. Jones, *J. Inst. Met.* **1933**, *51*, 131.
[26] S. Samson in *Structural Chemistry and Molecular Biology* (Eds.: A. Rich, N. Davidson), Freeman, San Francisco, **1968**, pp. 687–717.
[27] E. Hellner, E. Koch, *Acta Crystallogr. Sect. A* **1981**, *37*, 1.
[28] B. Chabot, K. Cenzual, E. Parthé, *Acta Crystallogr. Sect. A* **1981**, *37*, 6.
[29] H. Nyman, B. G. Hyde, *Acta Crystallogr. Sect. A* **1981**, *37*, 11.
[30] E. Hellner, W. B. Pearson, *Z. Kristallogr.* **1987**, *179*, 175.
[31] G. Kreiner, H. F. Franzen, *J. Alloys Compd.* **1997**, *259*, 83.
[32] S. Samson, *Nature* **1962**, *195*, 259.
[33] S. Samson, *Acta Crystallogr.* **1964**, *17*, 491.
[34] S. Samson, *Acta Crystallogr.* **1967**, *23*, 586.
[35] G. Cordier, V. Müller, *Z. Kristallogr.* **1993**, *205*, 353.
[36] S. Samson, D. A. Hansen, *Acta Crystallogr. Sect. B* **1972**, *28*, 930.
[37] W. Blase, G. Cordier, T. Vogt, *Z. Anorg. Allg. Chem.* **1991**, *606*, 79.
[38] G. Cordier, V. Müller, *Z. Naturforsch. B* **1994**, *49*, 721.
[39] M. L. Fornasini, B. Chabot, E. Parthé, *Acta Crystallogr. Sect. B* **1978**, *34*, 2093.
[40] M. Tillard-Charbonnel, C. Belin, *Mater. Res. Bull.* **1992**, *27*, 1277.
[41] A. Chahine, M. Tillard-Charbonnel, C. Belin, *Z. Kristallogr.* **1995**, *210*, 80.
[42] M. H. Booth, J. K. Brandon, R. Y. Brizard, C. Chieh, W. B. Pearson, *Acta Crystallogr. Sect. B* **1977**, *33*, 30.
[43] A. S. Koster, J. C. Schoone, *Acta Crystallogr. Sect. B* **1981**, *37*, 1905.
[44] S. Bobev, S. C. Sevov, *Inorg. Chem.* **2001**, *40*, 5361.
[45] S. Andersson, *Acta Crystallogr. Sect. B* **1980**, *36*, 2513.
[46] Q.-B. Yang, S. Andersson, L. Stenberg, *Acta Crystallogr. Sect. B* **1987**, *43*, 14.
[47] W. Hume-Rothery, G. V. Raynor, *The Structure of Metals and Alloys*, Institute of Metals, London, **1962**.
[48] N. F. Mott, H. Jones, *The Theory of the Properties of Metals and Alloys*, Dover, New York, **1958**.
[49] J. K. Burdett, *Chemical Bonding in Solids*, Oxford University Press, New York, **1995**.
[50] L. M. Hoistad, S. Lee, *J. Am. Chem. Soc.* **1991**, *113*, 8216.
[51] M. Tillard-Charbonnel, A. Manteghetti, C. Belin, *Inorg. Chem.* **2005**, *44*, 512.
[52] Q. Lin, J. D. Corbett, *Inorg. Chem.* **2005**, *44*, 512.
[53] B. G. Hyde, S. Andersson, *Inorganic Crystal Structures*, Wiley, New York, **1989**.
[54] R. L. Johnston, R. Hoffmann, *Z. Anorg. Allg. Chem.* **1992**, *616*, 105.
[55] Instances of ambiguity in the assignment of atoms to diamondoid and truncated-tetrahedral nets were noticed by Samson for the structures we focus on in this paper, $Mg_{17}Al_{12}$ and $NaCd_2$. See reference [26].
[56] H. C. Longuet-Higgins, C. W. Rector, J. R. Platt, *J. Chem. Phys.* **1950**, *18*, 1174.
[57] B. M. Gimarc, *J. Am. Chem. Soc.* **1983**, *105*, 1979.

[58] H. F. Franzen, M. Köckerling, *Prog. Solid State Chem.* **1995**, *23*, 265.
[59] G. J. Miller, *Eur. J. Inorg. Chem.* **1998**, 523.
[60] C. S. Lee, G. J. Miller, *Inorg. Chem.* **2001**, *40*, 338.
[61] B. Li, J. D. Corbett, *Inorg. Chem.* **2004**, *43*, 3582.
[62] P. Villars, L. D. Calvert, *Pearson's Handbook of Crystallographic Data for Intermetallic Phases*, *2nd ed.*, ASM, Materials Park, **1991**.
[63] T. F. Fässler, C. Kronseder, M. Wörle, *Z. Anorg. Allg. Chem.* **1999**, *625*, 15.
[64] W. Schaefer, K. H. J. Buschow, *Mater. Sci. Forum* **2004**, *443–444*, 263.
[65] R. Steadman, P. M. Nuttal, *Acta Crystallogr.* **1964**, *17*, 62.
[66] P. I. Krypyakevich, Y. B. Kuzma, V. S. Protasov, *Dopov. Akad. Nauk Ukr. RSR* **1963**, *4*, 492.
[67] W. Trzebiatowski, J. Niemic, *Rocz. Chem.* **1955**, *29*, 277.
[68] F. Bonhomme, K. Yvon, *J. Alloys Compd.* **1996**, *232*, 271.
[69] J. F. Smith, D. M. Bailey, D. B. Novotny, J. E. Davison, *Acta Metal.* **1965**, *13*, 889.
[70] One of us, D.C.F, is currently investigating with Sven Lidin at Stockholm University hints that additional disorder phenomena may be present in $NaCd_2$.
[71] We resisted inventing an abbreviation for these cluster building blocks based on "Recognizable Ordered Array of Lower Dimensionality".
[72] A. Simon, *Coord. Chem. Rev.* **1997**, *163*, 253.
[73] A. Simon, *Z. Anorg. Allg. Chem.* **1977**, *431*, 5.
[74] W. Dmowski, T. Egami, K. E. Swider-Lyons, C. T. Love, D. R. Rolison, *J. Phys. Chem. B* **2002**, *106*, 12677.
[75] U. Schwarz, *Z. Kristallogr.* **2004**, *219*, 376.
[76] M. McMahon, R. Nelmes, *Z. Kristallogr.* **2004**, *219*, 742.
[77] C. Hejny, L. F. Lundegaard, S. Falconi, M. I. McMahon, M. Hanfland, *Phys. Rev. B* **2005**, *71*, 020101.
[78] H. Fujihisa, Y. Akahama, H. Kawamura, Y. Gotoh, H. Yamawaki, M. Sakashita, S. Takeya, K. Honda, *Phys. Rev. B* **2005**, *72*, 132103.
[79] R. J. Nelmes, D. R. Allan, M. I. McMahon, S. A. Belmonte, *Phys. Rev. Lett.* **1999**, *83*, 4081.
[80] S. T. Hyde, S. Andersson, *Z. Kristallogr.* **1984**, *168*, 221.
[81] S. T. Hyde, S. Andersson, *Z. Kristallogr.* **1985**, *170*, 225.
[82] R. Nesper, H. G. von Schnering, *Angew. Chem.* **1986**, *98*, 111; *Angew. Chem. Int. Ed. Engl.* **1986**, *25*, 110.
[83] H. G. von Schnering, R. Nesper, *Angew. Chem.* **1987**, *99*, 1097; *Angew. Chem. Int. Ed. Engl.* **1987**, *26*, 1059.
[84] S. Hyde, S. Andersson, K. Larsson, Z. Blum, T. Landh, S. Lidin, B. W. Ninham, *The Language of Shape; The Role of Curvature in Condensed Matter: Physics, Chemistry and Biology*, Elsevier, Amsterdam, **1997**.
[85] S. Andersson, K. Larsson, M. Larsson, M. Jacob, *Biomathematics; Mathematics of Biostructures and Biodynamics*, Elsevier, Amsterdam, **1999**.
[86] F. S. Bates, G. H. Fredrickson, *Annu. Rev. Phys. Chem.* **1990**, *41*, 525.
[87] I. W. Hamley, *The physics of block copolymers*, Oxford University Press, New York, **1998**.
[88] K. Cenzual, E. Parthé, *Acta Crystallogr. Sect. C* **1986**, *42*, 14.
[89] G. Kresse, J. Hafner, *Phys. Rev. B* **1993**, *47*, 558.
[90] G. Kresse, J. Hafner, *Phys. Rev. B* **1994**, *49*, 14251.
[91] G. Kresse, J. Furthmüller, *Comput. Mater. Sci.* **1995**, *6*, 15.
[92] G. Kresse, J. Furthmüller, *Phys. Rev. B* **1996**, *54*, 11169.
[93] H. J. Monkhorst, J. F. Pack, *Phys. Rev. B* **1976**, *13*, 5188.
[94] D. Vanderbilt, *Phys. Rev. B* **1990**, *41*, 7892.
[95] G. A. Landrum, YAeHMOP is freely available on the WWW at URL: http://sourceforge.net/projects/yaehmop/.
[96] J. T. Schmidt, S. Lee, D. C. Fredrickson, M. Conrad, J. Sun, B. Harbrecht, *Chem. Eur. J.* **2007**, *13*, 1394.

